



**UNIVERSIDAD DE INVESTIGACIÓN DE
TECNOLOGÍA EXPERIMENTAL YACHAY**

ESCUELA DE CIENCIAS FÍSICAS Y NANOTECNOLOGÍA

**TÍTULO: Synthesis and Characterization of Samarium
Doped-Hydroxyapatite and Preliminary Cytotoxicity Study**

Trabajo de integración curricular presentado como requisito para
la obtención del título de Ingeniera en Nanotecnología

Autor:

Enríquez Olivo Stephanie Nicole

Tutor:

Ph.D. – González Vásquez Gema

Co-Tutor:

Ph.D. – Briceño Araujo Sarah

Ph.D. – Ramírez Cando Lenin

Urququí, mayo 2024

AUTORÍA

Yo, **ENRÍQUEZ OLIVO STEPHANIE NICOLE**, con cédula de identidad 1721746913, declaro que las ideas, juicios, valoraciones, interpretaciones, consultas bibliográficas, definiciones y conceptualizaciones expuestas en el presente trabajo; así como, los procedimientos y herramientas utilizadas en la investigación, son de absoluta responsabilidad de el/la autora (a) del trabajo de integración curricular. Así mismo, me acojo a los reglamentos internos de la Universidad de Investigación de Tecnología Experimental Yachay.

Urcuquí, mayo 2024.

Stephanie Nicole Enríquez Olivo

CI: 1721746913

AUTORIZACIÓN DE PUBLICACIÓN

Yo, **ENRÍQUEZ OLIVO STEPHANIE NICOLE**, con cédula de identidad 1721746913, cedo a la Universidad de Investigación de Tecnología Experimental Yachay, los derechos de publicación de la presente obra, sin que deba haber un reconocimiento económico por este concepto. Declaro además que el texto del presente trabajo de titulación no podrá ser cedido a ninguna empresa editorial para su publicación u otros fines, sin contar previamente con la autorización escrita de la Universidad.

Asimismo, autorizo a la Universidad que realice la digitalización y publicación de este trabajo de integración curricular en el repositorio virtual, de conformidad a lo dispuesto en el Art. 144 de la Ley Orgánica de Educación Superior

Urcuquí, mayo 2024.

Stephanie Nicole Enríquez Olivo

CI: 1721746913

Dedication

I dedicate this thesis to my beloved family, who have nurtured in me solid values and taught me the importance of honesty, perseverance, and respect. Their unwavering love and support have served as the pillar upon which I have built this achievement. To my parents, for their sacrifice, patience, and constant encouragement. To my sisters, for their companionship, laughter, and ever-willing assistance. To my friends, for consistently standing by my side, offering their friendship and unwavering support. To my teachers and mentors, for their invaluable guidance and wisdom. I extend my gratitude to all who believed in me, for being an integral part of this chapter in my life.

Stephanie Nicole Enríquez Olivo

Acknowledgements

I would like to express my sincere gratitude to my advisor, Prof. Gema Gonzalez, as well as my co-advisor, Prof. Sarah Briceño, for their patience, guidance, and support throughout the completion of this research. With their profound knowledge and heartwarming attitude, both have inspired the person and professional I aspire to become. I would also like to express my gratitude to my co-advisor, Prof. Lenin Ramirez, for having the patience and motivation to guide me through the complexity of cell biology.

I extend my gratitude to my fellow classmates and friends with whom I shared these unforgettable years filled with challenges, experiences, and enjoyment. In particular, I would like to express a special thanks to Anderson, Ana Gabriela, Ariel, Christian, Eduardo, Nardy, Juan, Antonio, Pablo, Leonel, Saul, and Patricio for being exceptional individuals I had the opportunity to cross paths. Additionally, I extend profound gratitude to Gabriela for the extended working hours in the laboratory. It's her contagious perseverance that made this work possible.

I also express my thanks to Yomaira, Fernando, Laila, and Josue for their invaluable friendship. Each one of you made my university life beautiful, and I am profoundly thankful for the connection and moments we shared. Special thanks to Dario for accompanying me during the last months of my academic journey. I will cherish these memories dearly.

Finally, I would like to extend my heartfelt gratitude to my family for their unconditional love and unwavering support throughout my life's journey. To my parents, whose encouragement and motivation have empowered me to turn my dreams into reality. Thank you for following each one of my steps with excitement. To my younger sisters, for being the best friends I could ever wish for.

Stephanie Nicole Enríquez Olivo

Resumen

La hidroxiapatita (HAp) es un biomaterial ampliamente utilizado en aplicaciones biomédicas y el principal componente del tejido óseo. Este compuesto inorgánico tiene una gran afinidad por las sustituciones iónicas, lo que mejora sus ya notables propiedades. Al sustituir los iones Ca^{2+} por lantánidos, el material adquiere características ópticas, antimicrobianas y biológicas mejoradas. En particular, el samario (Sm) muestra una fuerte afinidad por los minerales óseos. Esta investigación se centra en la síntesis de hidroxiapatita dopada con samario (Sm:HAp; $\text{Ca}_{10-x}\text{Sm}_x(\text{PO}_4)_6(\text{OH})_2$) con concentraciones específicas de Sm ($x = 0.05, 0.1, 0.5$ y 1.0), sometida a calcinación a diferentes temperaturas (200°C , 400°C , 600°C y 800°C). Las técnicas de caracterización, incluyendo espectroscopía infrarroja por transformada de Fourier, espectroscopía Raman y difracción de rayos X (DRX), confirmaron la integración exitosa de los iones Sm^{3+} en la estructura de la HAp sin alterar su disposición cristalina. La espectroscopía de fotoluminiscencia mostró un aumento en la intensidad de la luminiscencia en muestras sometidas a calcinación a altas temperaturas. La viabilidad celular de la Sm:HAp sintetizada fue evaluada mediante estudios de citotoxicidad, utilizando los ensayos de exclusión de colorante azul de Tripán y MTT. Los resultados revelaron una disminución de la viabilidad celular dependiente de la concentración en células de neuroblastoma. Esta investigación destaca el potencial de la Sm:HAp como un material biocompatible con propiedades mejoradas.

Palabras Clave: Hidroxiapatita, Samario, Dopaje, Fotoluminiscencia, Citotoxicidad, Viabilidad Celular.

Abstract

Hydroxyapatite (HAp) is a commonly used biomaterial in biomedical applications and the main constituent of bone tissue. This inorganic compound exhibits an affinity for substitutions, enhancing its already unique properties. By replacing Ca^{2+} ions with lanthanides, the material gains improved optical, antimicrobial, and biological characteristics. In particular, samarium (Sm) possesses a strong affinity for bone minerals, making it suitable for bio-imaging and drug-delivery systems. This research focuses on synthesizing samarium-doped hydroxyapatite (Sm:HAp; $\text{Ca}_{10-x}\text{Sm}_x(\text{PO}_4)_6(\text{OH})_2$) with specific Sm concentrations ($x = 0.05, 0.1, 0.5, \text{ and } 1.0$) and subjected to calcination at varying temperatures ($200^\circ\text{C}, 400^\circ\text{C}, 600^\circ\text{C}, \text{ and } 800^\circ\text{C}$). Characterization techniques, including Fourier-transform infrared spectroscopy (FTIR), Raman spectroscopy, and x-ray diffraction (XRD) confirmed the successful integration of Sm^{3+} ions into the HAp structure without disrupting its crystalline arrangement. Photoluminescence spectroscopy highlighted increased luminescence intensity in samples subjected to high-temperature calcination. The cell viability of the synthesized Sm:HAp was assessed through cytotoxicity studies, employing Trypan Blue Dye Exclusion and MTT assays. Results revealed a concentration-dependent decrease response of viability in neuroblastoma cells. This research emphasizes the potential of Sm:HAp as a biocompatible material with enhanced properties.

Keywords: Hydroxyapatite, Samarium, Doping, Photoluminescence, Cytotoxicity, Cell Viability.

Contents

List of Figures	xii
List of Tables	xiv
1 Introduction	1
1.1 Problem Statement	2
1.2 General and Specific Objectives	2
1.2.1 General Objective	2
1.2.2 Specific Objectives	2
2 Theoretical Background	3
2.1 Nanotechnology	3
2.1.1 Nanomedicine	3
2.2 Hydroxyapatite	4
2.2.1 Hydroxyapatite Substitutional Doping	5
2.2.2 Synthesis of Hydroxyapatite	5
2.3 Samarium	6
2.4 Luminescence	7
2.4.1 Photoluminescence	7
2.5 Cell Viability and Cytotoxicity	9
2.5.1 Trypan Blue Exclusion Method	10
2.5.2 MTT Assay	10
2.6 SH-SY5Y Neuroblastoma Cell Line	11
2.7 State of the Art	11
2.8 Characterization Techniques	12
2.8.1 Fourier Transform Infrared Spectroscopy	12
2.8.2 Raman Spectroscopy	14
2.8.3 X-Ray Diffraction	15

2.8.4	Photoluminescence Spectroscopy	16
2.8.5	Scanning Electron Microscopy	16
3	Methodology	19
3.1	Synthesis of the Biomaterial	19
3.1.1	Reagents	19
3.1.2	Hydroxyapatite (HAp) and Samarium Doped Hydroxyapatite (Sm:HAp)	19
3.2	Characterization	20
3.2.1	Fourier Transform Infrared Spectroscopy	21
3.2.2	Raman Spectroscopy	21
3.2.3	X-Ray Diffraction	21
3.2.4	Scanning Electron Microscopy	21
3.2.5	Photoluminescence Spectroscopy	21
3.3	Cytotoxicity Study	22
3.3.1	Reagents	22
3.3.2	Procedure	22
4	Results & Discussion	25
4.1	Structural Characterization	25
4.1.1	Fourier Transform Infrared Spectroscopy	25
4.1.2	Raman Spectroscopy	27
4.1.3	X-ray Diffraction	30
4.2	Optical Characterization	32
4.2.1	Photoluminescence Spectroscopy	32
4.3	Morphological Characterization	34
4.3.1	Scanning Electron Microscopy	34
4.4	Cytotoxicity Studies	37
4.4.1	Trypan Blue	37
4.4.2	MTT Assay	39
5	Conclusions & Outlook	41
A	Additional Information	43
	Bibliography	47

List of Figures

2.1	Crystal Structure of Hexagonal Hydroxyapatite	5
2.2	Luminescence Jablonski Diagram	8
2.3	Principle of MTT Assay	10
2.4	Undifferentiated and differentiated SH-SY5Y cells	11
2.5	Fourier transform infrared spectrometer scheme	13
2.6	Rayleigh and Raman Scattering Processes	14
2.7	X-ray Diffractometer Scheme	15
2.8	Electron - matter interaction volume.	17
3.1	Hydrothermal synthesis method of Sm:HAp samples	20
3.2	Trypan Blue Exclusion Test Protocol	23
3.3	MTT Assay Protocol	24
4.1	FTIR spectra of Sm:HAp samples at room temperature	26
4.2	FTIR spectra of Sm:HAp samples at different calcination temperatures (200 °C, 400 °C, 600 °C, and 800 °C).	27
4.3	Raman spectra of Sm:HAp samples at room temperature	28
4.4	Raman spectra of Sm:HAp samples at different calcination temperatures (200 °C, 400 °C, 600 °C, and 800 °C).	29
4.5	XRD pattern of Sm:HAp samples at room temperature	30
4.6	XRD pattern of Sm:HAp samples at different calcination temperatures (200 °C, 400 °C, 600 °C, and 800 °C).	31
4.7	PL spectra of Sm:HAp samples at room temperature	33
4.8	PL spectra of Sm:HAp samples at different calcination temperatures (200 °C, 400 °C, 600 °C, and 800 °C).	34
4.9	SEM images of uncalcined and calcined Sm:HAp samples at 800 °C.	35
4.10	EDS microanalysis of Sm:HAp samples at room temperature	36
4.11	Elemental mapping of Sm:HAp ($x_{Sm} = 0.5$) samples at room temperature	37

4.12	Biocompatibility assessment using Trypan Blue Dye Exclusion test: percentage of viable SH-SY5Y cells after a 24-hour incubation with Sm:HAp samples	38
4.13	Biocompatibility assessment using MTT assay: percentage of viable SH-SY5Y cells after a 24-hour incubation with Sm:HAp samples	40
A.1	Trypan Blue and MTT assays treatment positions.	45

List of Tables

3.1	Concentration and masses of the compounds following the fixed $(\text{Ca}+\text{Sm})/\text{P} = 1.67$	20
A.1	Phase analysis for Sm:HAp samples calcined at 800 °C.	43
A.2	PL peak intensities of Sm:HAp samples ($x_{\text{Sm}}=0, 0.05, 0.1, 0.5, 1.0$) at different calcination temperatures	44

Chapter 1

Introduction

Utilizing nanomaterials for medical purposes has offered innovative solutions to address current healthcare challenges. Hydroxyapatite is a renowned biomaterial in the medical realm due to its unique biological properties, including low toxicity, biocompatibility, bioactivity, and osteoconductivity^{1,2}. Essentially, hydroxyapatite is a calcium phosphate compound naturally found in hard tissues like bone and teeth in both animals and humans^{3,4}. It typically exhibits a hexagonal structure with $P6_3/m$ symmetry group and has an affinity for ionic substitutions that can enhance its physicochemical and biological characteristics. By introducing anionic and cationic substitutions for therapeutic ions, it is possible to improve its antibacterial properties and inhibit osteoclast activity. This opens up diverse applications, such as serving as delivery carriers, imaging contrast agents⁵, and coatings for implants.

Lanthanide elements can substitute Ca^{2+} ions in the hydroxyapatite structure⁶. Specifically, trivalent lanthanide ions (Ln^{3+}) possess distinctive electromagnetic and optical properties, attributed to the presence of unpaired electrons in the 4f orbitals⁷, making them well-suited for applications in biology. Among these, samarium, an abundant element in the lanthanide series, stands out for its luminescence, radioactive nature, antimicrobial activity, and high affinity to bone mineral³. This study aims to incorporate Sm^{3+} ions into the hydroxyapatite lattice structure and evaluate the biocompatibility of this compound through cytotoxicity assays.

Samarium-doped hydroxyapatite has been effectively tested on various cell lines, including HGF-1 gingival fibroblasts⁷, hFOB 1.19 osteoblasts⁶, and HeLa cervical cancer-derived cells⁴. The cellular behavior and response are dependent upon the concentration of Sm content. In this study, the SH-SY5Y neuroblastoma cell line is selected due to its ease of experimentation, straightforward analysis, and established standardized use. SH-SY5Y cells are commonly employed in in-vitro research to model neurodegenerative diseases such as Parkinson's and Alzheimer's⁸. Importantly, these cells are relevant for investigating cellular responses and cytotoxic effects of various treatments, particularly in the context of neural tissues and cancer cells.

1.1 Problem Statement

The application and development of nanomaterials in the medical field introduce several challenges. The interest in creating biologically active luminescent materials has grown due to their promising multifunctional applications. Yet, a primary concern hindering their clinical use is the potential toxicity of these nanomaterials.

1.2 General and Specific Objectives

1.2.1 General Objective

To synthesize luminescent and biocompatible samarium-doped hydroxyapatite (Sm:HAp) through substitutional doping, and to analyze its structural characteristics and preliminary biocompatibility and cytotoxicity studies.

1.2.2 Specific Objectives

- To synthesize stoichiometric hydroxyapatite through the hydrothermal method.
- To replace divalent calcium ions (Ca^{2+}) with trivalent samarium ions (Sm^{3+}) in the hydroxyapatite lattice structure, producing samples with different samarium content.
- To perform heat treatments at different temperatures.
- To characterize the structure, morphology, composition, and optical properties of samples through FTIR, Raman spectroscopy, XRD, SEM, EDS, and PL spectroscopy techniques.
- To evaluate the biocompatibility and cytotoxic effects of Sm:HAp samples on SH-SY5Y cell lines.

Chapter 2

Theoretical Background

2.1 Nanotechnology

Nanotechnology is an emerging branch of science for manipulating and designing structures, devices or systems at nanoscale size (1 – 100 nm). When materials are at the nanometer scale, they exhibit unique physical, chemical, and biological properties that differ from those of individual atoms, molecules, and bulk materials⁹. These phenomena occur in nanomaterials because of two main factors including the high surface area to volume ratio and the quantum effects that predominate over classical physics^{9,10}. As a result, their chemical reactivity along with their mechanical, electrical, optical, magnetic, and structural properties can be significantly influenced opening up opportunities for novel applications in several fields such as medicine with drug delivery, bioimaging, disease diagnosis, analysis, and treatment; in electronics with enhanced semiconductor devices; in energy with more efficient solar cells and energy storage devices; in environmental sustainability, and materials science.

2.1.1 Nanomedicine

Nanomedicine refers to the utilization of nanomaterials for diagnosis, monitoring, control, prevention, and treatment of diseases and injuries¹¹. In other words, nanomedicine describes the use of nanotechnology in the field of medicine. The nanometric scale and surface-to-volume ratio of nanomaterials play a fundamental role, particularly in many biological mechanisms and structures within the human body. These dimensions allow them to potentially cross biological barriers, accessing previously unreachable delivery sites and various cellular compartments¹² at diverse levels within the blood, organs, or tissues. In addition, nanomaterials can be engineered to facilitate the interaction with specific biological targets¹¹, which determine the biocompatibility, stability, performance, and side effects of the material¹³. This enables the creation of tools for diagnostic and analysis, vehicles for delivering drugs¹⁴, constructs for tissue engineering, and implants¹⁵. For instance, nanostructured materials such as metal NPs, liposomes, dendrimers, carbon nanotubes, and micelles are considered potential drug-delivery carriers in treating brain cancer. Their unique nanoscale dimensions enable effective transportation and seamless passage across the blood-brain

barriers (BBBs) leading to a reduction in required drug concentrations and also facilitating safer drug administration in contrast to conventional drug dosages¹⁶. Therefore, nanomedicine introduces an innovative approach to healthcare treatments.

2.2 Hydroxyapatite

Hydroxyapatite (HAp), with the chemical formula $\text{Ca}_{10}(\text{PO}_4)_6(\text{OH})_2$, is a naturally occurring mineral form of calcium apatite. Its crystalline structure consists of 39.84 % calcium ions, 56.77 % phosphate ions, and 3.39 % hydroxyl ions¹⁷, maintaining the Ca/P = 1.67. Hydroxyapatite is a primary inorganic component in biological systems, particularly in bones, teeth, and enamel¹⁸. Specifically, in the context of bone formation, HAp, along with collagen, proteins, and water, plays a crucial role. In this process, HAp exists as plate-like crystals in the nanometer size, aligned parallel to the collagen fibers which serve as a matrix¹⁹. These crystals provide bones with strength and rigidity. Furthermore, HAp is also present in igneous, sedimentary, and metamorphic rocks, making it the most abundant phosphorus-bearing mineral²⁰.

In terms of crystalline structure, hydroxyapatite exists in two phases: a monoclinic form in the $P2_1/b$ space group and a hexagonal form in the $P6_3/m$ space group, which is the more common phase. Impurities and foreign atoms easily destabilized the monoclinic form. The hexagonal form presents the following lattice parameters: physical dimensions $a = b = 9.418 \text{ \AA}$, $c = 6.884 \text{ \AA}$, and angles $\alpha = \beta = 90^\circ$, $\gamma = 120^\circ$ ¹⁹. This structure comprises two distinct calcium sites, labeled Ca(I) as the columnar Ca and Ca(II) as the screw axis Ca²¹. Within this structure, a phosphate arrangement forms two separate channels along the crystallographic c-axis, known as channel A and channel B. Channel A is positioned at a crystal height of $\frac{1}{4}$, while channel B is located at a height of $\frac{3}{4}$ ¹⁷. These channels are conduits filled with hydroxyl ions, which align with the c-axis¹⁹. Ca(I) sites are organized in vertical columns that run parallel to the OH^- channels. In contrast, Ca(II) sites follow an equilateral triangle pattern, perpendicular to the OH^- channels. These Ca(II) sites are precisely positioned on the $z = \frac{1}{4}$ and $z = \frac{3}{4}$ mirror planes and are rotated 60° about the c-axis^{22,23}. This arrangement contributes to the distinctive structural characteristics of HAp (Figure 2.1).

The crystalline structure, morphology, stoichiometric ratio, and particle size of HAp are fundamental factors that determine its physical, chemical, and biological properties²⁵, rendering it an exceptional material across multiple fields. These properties make HAp particularly valuable in the medical realm, the chemical industry, and environmental remediation. It possesses remarkable traits, including biocompatibility, bioactivity, non-toxicity, thermal stability, ion exchange capabilities, and absorption capacity²⁶. Consequently, HAp is a preferred option for applications such as bone repair materials, implant coatings, drug delivery carriers, photocatalysts, biosensors, and membranes designed for heavy metal removal from polluted water²⁵. Additionally, HAp exhibits lattice flexibility, allowing for substitutional doping.

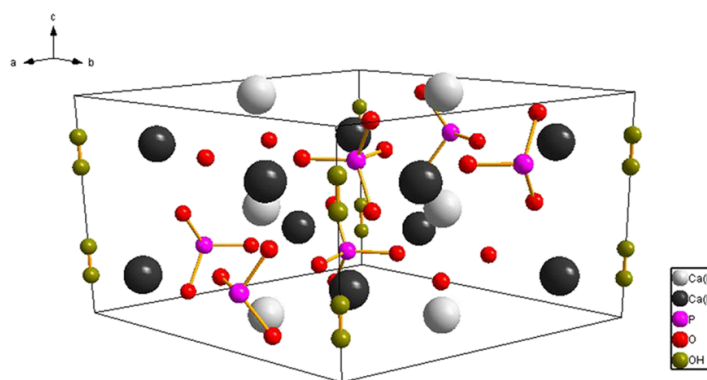


Figure 2.1: Crystal Structure of Hexagonal Hydroxyapatite. Retrieved from Zhu, Y, et al. (2018)²⁴.

2.2.1 Hydroxyapatite Substitutional Doping

The flexibility of the hexagonal structure of hydroxyapatite accommodates ionic substitutions for the Ca^{2+} , PO_4^{3-} , and OH^- groups. Cationic substitutions occur at calcium sites, while anionic substitutions may involve either the phosphate sites, the hydroxyl sites, or both¹⁷. Calcium ions can be substituted with iso-, mono-, and multi-valent ions as Na^+ , Sr^{2+} , Mg^{2+} , Mn^{2+} , Ga^{3+} , Ti^{4+} , as well as lanthanides like $\text{Ce}^{3+/4+}$, and Eu^{3+} ¹⁹. Besides, anionic substitutions for phosphate and hydroxyl groups typically include CO_3^{2-} , SiO_4^{4-} , SeO_3^{2-} , F^- , and Cl^- ⁵. Carbonate substitutions are common in hydroxyapatite, involving A-type (OH^-), B-type (PO_4^{3-}), and AB-type replacements¹⁸. The incorporation of these foreign ions within the lattice can affect the crystal structure, crystallinity, morphology, mechanical properties, solubility, thermal stability, biological activity, and biological response^{21,27}. This offers valuable insight for various applications.

2.2.2 Synthesis of Hydroxyapatite

Hydroxyapatite can be obtained from both natural sources and synthesized artificially. Natural hydroxyapatite is found in various sources, including those of mammalian, aquatic, and mineral origins, such as bones, teeth, shells, geological deposits, and marine organisms. The quality and purity of natural HAp may vary depending on its source and the processing methods employed, as it may contain trace elements like Na^+ , K^+ , Zn^{2+} , Mg^{2+} , Si^{4+} , Ba^{2+} , F^- , and CO_3^{2-} . This composition closely resembles that of human bone²⁸.

Synthetic hydroxyapatite can be obtained through various methods, including dry methods such as solid-state and mechanochemical techniques, wet methods like chemical precipitation, hydrolysis, sol-gel, hydrothermal, emulsion, and sonochemical processes, as well as high-temperature methods such as combustion and pyrolysis^{28,29}. The choice of synthesis method depends on the desired properties and specific application.

Wet methods are the most frequently employed techniques for synthesizing HAp. These methods rely on solution-based chemical reactions, which can be conducted at ambient or elevated temperatures to produce HAp as a precipitate. These techniques offer advantages in controlling the morphology and size of the powder through the adjustment of reaction parameters²⁹. Despite their ease of operation, wet methods may introduce impurities and reduce crystallinity potentially leading to the formation of calcium phosphate phases³⁰.

Hydrothermal Method

Hydrothermal synthesis is a significant method for generating ceramic materials by utilizing high temperature and pressure within a closed system, such as an autoclave or pressure vessel^{30,31}. This method operates at pressures exceeding 100 kPa and temperatures ranging from above 25 °C³² to below 350 °C³³. This technique is versatile, as it can be employed to convert slurries, solutions, or gels into the desired crystalline phase³³. Specifically, hydroxyapatite is synthesized by subjecting calcium and phosphate precursors to controlled conditions.

Within this process, the combined influence of increased pressure and elevated temperature conditions enhances reactivity²⁹, promoting the interaction between calcium and phosphate ions and encouraging nucleation³⁰. The formation of nuclei arises from the creation of chemical bonds due to condensation effects²⁹. Factors as temperature and pH influence structural and morphological properties³⁰, meanwhile higher temperatures enhance phase purity and the Ca/P ratio¹⁷. The process duration is critical for effective crystal growth, ensuring high-quality hydroxyapatite production. The hydrothermal method typically produces samples with high crystallinity and relatively stoichiometric composition³⁰. However, these samples frequently exhibit inconsistent morphologies, with most assuming a spherical or rod-like shape, and a wide size distribution¹⁷. Controlled size and morphology can be achieved by introducing modifiers such as calcium chelating agents and various organic surfactants^{29,30}.

2.3 Samarium

Samarium (Sm) is a chemical element with an atomic number of 62, corresponding to the lanthanide series in the periodic table. The most stable oxidation state is Sm³⁺, but it can also exist Sm²⁺, where certain Sm(II) compounds act as strong single-electron reducing agents³⁴. It also possesses a relatively large atomic radius of 238 pm³⁵ with an ignition temperature of 150 °C and a melting point at 1074 °C. Physically, samarium appears as a moderately hard metal with a shiny silver luster and displays reasonable stability in ambient air³⁶. It exhibits three distinct crystal structures through temperature-induced transformations. At room temperature, samarium typically adopts a rhombohedral structure characterized by an ABABCBCACA stacking sequence. When heated to 731 °C, it transforms a hexagonal close-packed (hcp) structure, further transitioning into a body-centered cubic (bcc) structure at 922 °C³⁷.

Samarium is the 40th most abundant element in Earth's crust and it is commonly found in various minerals, primarily in monazite and bastnaesite, alongside other lanthanide metals. This metal was discovered in 1879 by the French chemist Paul-Émile Lecoq de Boisbaudran, who successfully extracted samarium from the mineral

samarskite. This mineral was originally discovered in the Ural Mountains and received its name in recognition of Colonel Vassili Samarsky-Bykhovets, a Russian mining official^{34,38}. The isolation of samarium from the remaining mineral components involves techniques such as ion exchange and solvent extraction. In fact, natural samarium (^{62}Sm) consists of seven stable isotopes, namely ^{144}Sm , ^{147}Sm , ^{148}Sm , ^{149}Sm , ^{150}Sm , ^{152}Sm , and ^{154}Sm , with ^{152}Sm being the most abundant at 26.74 %³⁹.

Some common uses for samarium compounds include their use in high-powered permanent magnets, especially in the form of samarium-cobalt magnets known for their strength and heat resistance, enabling the miniaturization of electronic devices. It is also employed in optical lasers, infrared-absorbing glass, as a neutron absorber in nuclear reactors, and in making glass, ceramics, and studio lighting for movies and projections³⁴.

2.4 Luminescence

Luminescence is the spontaneous emission of radiation observed in non-equilibrium systems, typically at normal or lower temperatures. This phenomenon is evident in nature through various organisms like glow-worms, fireflies, deep-sea animals, and certain sea-bacteria⁴⁰. Also, in catalytic reactions⁴¹ such as those involving luminol. Luminescence occurs when an external energy source excites an electron from its lowest-energy state (ground state) to a higher-energy state (excited state). Subsequently, the system undergoes relaxation processes to restore equilibrium, causing the excited electron to return to its ground state and release energy in the form of light. Intermediate processes occur between absorption and emission, influencing the duration of luminescence and the likelihood of quenching effects⁴².

Based on the emission duration (τ_c), luminescence falls into two categories: fluorescence and phosphorescence (Figure 2.2). Fluorescence emission has a brief lifetime after the removal of the energy source ($\tau_c < 10^{-8}$ s), whereas phosphorescence emission endures longer, persisting for hours ($\tau_c > 10^{-8}$ s)⁴¹. The latter is a temperature-dependent process and exhibits a delay in achieving maximum intensity⁴⁰. Luminescence can also be classified by the mode of excitation. Some examples include photoluminescence, induced by photon excitation; chemiluminescence, arising from chemical reactions; mechanoluminescence, triggered by mechanical energy; electroluminescence, responding to an electric field; and thermoluminescence, occurring during heating^{40,44}.

2.4.1 Photoluminescence

Photoluminescence (PL) is the emission of light initiated by photons during the process of photoexcitation. This term is a combination of the Latin-derived word "luminescence," and the Greek prefix "photo-" for light⁴⁵. The energy of the exciting photon, relative to the emitted light, can result in resonant or non-resonant excitation, where the wavelength is either equivalent or different from the incoming photon⁴⁶. The PL phenomenon can manifest in a diverse range of materials under suitable conditions, including atoms, molecules, polymers, aggregates, and crystals, whether they are organic or inorganic. The emitted light is an inherent attribute of the object⁴⁰.

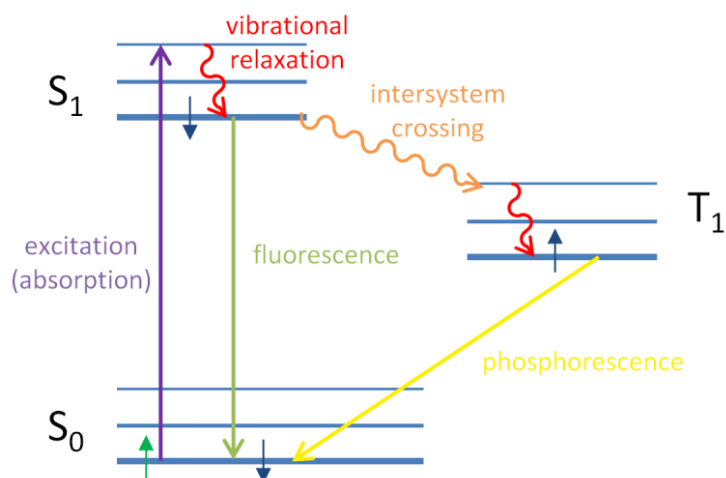


Figure 2.2: Jablonski diagram explaining the occurrence of fluorescence and phosphorescence. Retrieved from Eck, M (2014)⁴³.

Photoluminescence of Hydroxyapatite

Pure or stoichiometric hydroxyapatite does not exhibit luminescence^{47,48}. Instead, luminescent properties arise from modifications in the electronic configuration of HAp, attributed to the formation of structural defects or vacancies⁴⁷, or the introduction of dopants or impurities into the structure.

Changes in the electronic structure and charge distribution can lead to the creation of different energy levels within the band gap which may be responsible for the luminescent properties. Various factors such as heating effects causing the decomposition of entrapped species, the introduction of external components from the atmosphere, modifications in the lattice's crystallinity degree, and sintering processes, can promote these alterations⁴⁹. Additionally, the defective structure of HAp, where the presence of CO_3^{2-} ions and the movement and reorientation of OH^- ions in the c-channel, also attribute to these order-disorder changes⁵⁰. Synthesis processes can also induce alterations in the crystal structure, contributing to the formation of vacancies⁴⁷. Indeed, the ability to precisely control and manipulate these energy levels could allow the acquisition of tunable colors⁵⁰ obtaining blue and green emissions⁵¹.

In the context of impurities, HAp acts as a host matrix with the capacity to bind luminescent ions, referred to as luminescent centers, due to its adaptable lattice structure⁴⁹. Typically, transition metals and rare earth elements are incorporated as dopants to establish luminescent centers within the crystal structure⁴⁷.

Photoluminescence of Samarium

The luminescent properties of materials are related to their electronic band structure. Rare earth atoms exhibit a complex energy level arrangement, characterized by a xenon-like structure, a partially filled 4f shell, and two or three electrons in the 6s and 5d outer shells⁵². Typically, REEs are incorporated into materials in either the divalent or trivalent state. The ground electronic configuration for these ions is $4f^N$, and their first excited configuration is $4f^{N-1} 5d$ ⁵³. This specific electronic configuration implies that REEs are expected to fluoresce, primarily due to the transitions involving the 4f electrons.

REEs are commonly incorporated in matrices to regulate and optimize their luminescence. The crystal symmetry can influence the energy levels of REEs⁵⁴. When incorporated into complexes, lanthanides present unique features, including narrow emission bands, a significant Stoke's shift, extended emission lifetimes, enhanced luminescence⁵⁵, and the capability to generate pure emission⁵⁶.

Particularly, the fluorescence of samarium ions (Sm^{3+}) is observed in the visible and near-infrared regions. Primarily, they emit orange-red light through transitions from the $^4G_{5/2}$ state to the 6H_J states ($J = 5/2, 7/2, 9/2, \text{ and } 11/2$)^{56,57}, corresponding to the 570, 610, 650, and 720 nm bands in the visible emission spectrum. Sm^{3+} exhibits a complex energy level structure with ground-state multiplets 6H_J and 6F_J , along with an excited state $^6G_{5/2}$ ⁵⁸. In contrast to Eu^{3+} ions, Sm^{3+} exhibits a diminished luminescence quantum yield, leading to a reduced luminescence intensity⁵⁹. This phenomenon arises from the closely spaced excited states which promote non-radiative decay processes, in addition to a smaller energy gap between the emitting state and the ground state⁶⁰.

2.5 Cell Viability and Cytotoxicity

Cell viability is the proportion of healthy living cells within a given population. In vitro cell viability assays are crucial for determining cell survival, proliferative capacity, and metabolic activity, as well as for detecting apoptosis within a cultured population. Additionally, these assays serve as indicators of a cell's response to specific drugs or chemical agents⁶¹. A compound or substance that induces damage or death to cells is labeled as cytotoxic. As a consequence, cytotoxicity assays are employed as screening tests to identify substances or conditions that potentially have toxic effects on cells. These effects are observed and measured through induced alterations in the cell proliferation rate, reproduction, structural integrity^{62,63}, and metabolic pathways⁶⁴.

Multiple techniques are used for assessing cell viability and detecting cytotoxicity effects. These methods may depend on various cellular functions such as cell membrane permeability, dye uptake, metabolic activities, enzyme releasing, cell adherence, ATP production, co-enzyme productions, DNA synthesis, and nucleotide uptake activity⁶¹. The effectiveness of evaluating cytotoxicity and cell viability depends on the chosen method, which is influenced by factors such as cell type, culture conditions, intended application, and sample characteristics^{61,63}.

2.5.1 Trypan Blue Exclusion Method

Dye exclusion methods are traditional techniques in cell biology that are employed to evaluate cell viability by distinguishing between viable and nonviable cells or tissues through staining. The dye used is impermeable to normal cells but permeable to dead cells due to a damaged plasma membrane. Therefore, these assays rely on the breakdown in membrane integrity, which is typically impermeable. Commonly used dyes for differentiation include Trypan Blue, Erythrosin B, or Naphthalene Black⁶⁵. Trypan Blue, an anionic hydrophilic azo dye with the molecular formula $C_{34}H_{24}N_6Na_4O_{14}S_4$, is utilized in both in vitro and in vivo analysis. Its ability to cross the cell membranes of dead cells allows it to stain the cytoplasm with a distinct blue color⁶⁶ by binding with intracellular proteins. Live cells, on the other hand, remain unstained and exhibit a round shape with a smaller size compared to dead cells⁶⁷. In the analysis, the cell suspension is observed under a light microscope, and cells are manually counted using a hemocytometer. While this technique allows for calculating the number and percentage of viable cells, its limited sensitivity prevents the recognition of apoptosis and necrosis⁶¹.

2.5.2 MTT Assay

Metabolic cell proliferation assays measure the metabolic activity as a reflection of the culture conditions. Metabolically active cells demonstrate the capacity to reduce tetrazolium salts like MTT (3-(4,5-dimethylthiazol-2-yl)-2,5-diphenyltetrazolium bromide), XTT (2,3-bis(2-methoxy-4-nitro-5-sulfophenyl)-2H-tetrazolium-5-carboxanilide), and WST-1 (3-(4-nitrophenyl)tetrazol-2-ium-5-yl]benzene-1,3-disulfonate) to form formazan. These compounds undergo reduction facilitated by oxidized substrates or specific enzymes, including NADH and NADPH⁶⁸. Specifically, the MTT reagent is a yellow mono-tetrazolium salt, and its reduction disrupts the tetrazole ring, resulting in the formation of formazan, a water-insoluble violet-blue molecule⁶⁹, as observed in Figure 2.3. The reduction of MTT is catalyzed by succinate dehydrogenase, an enzyme intricately involved in the mitochondrial electron transport system⁶⁸. Consequently, the MTT assay assesses the number of viable cells by quantifying the amount of formazan crystals produced due to their mitochondrial activity⁶¹. The formazan concentration is determined using a spectrophotometer after dissolution in an organic solvent such as dimethyl sulfoxide or detergent dodecyl sulfate^{61,68}. The most common use for MTT assay is to detect the cytotoxic effects of different agents under different conditions.

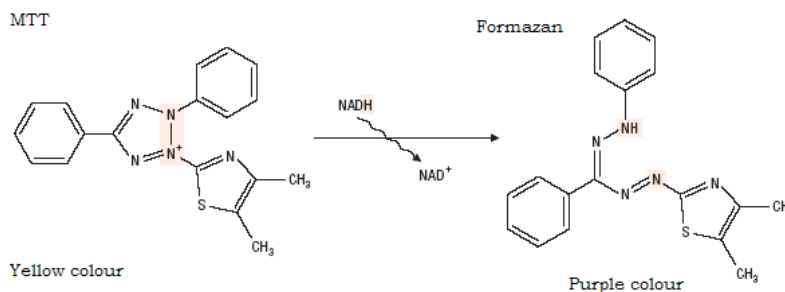


Figure 2.3: Principle of MTT-assay. Retrieved from Desai, S, et al. (2011)⁷⁰.

2.6 SH-SY5Y Neuroblastoma Cell Line

Neuroblastoma cell lines are transformed cells originating from the neural crest that retain the capacity for proliferation and differentiation in culture. These cell lines are widely used in scientific research for testing neurotoxicity, understanding virus-host cell interactions, and probing interrelations among cellular processes⁷¹. In particular, SH-SY5Y is a human-derived neuroblastoma cell line subcloned from the parental cell line SK-N-SH, which was isolated from a bone marrow biopsy of a four-year old female patient in the early 1970's^{72,73}. SH-SY5Y cells can undergo differentiation (Figure 2.4) into mature human neurons through treatment with various agents, including retinoic acid, purine, and staurosporine⁷³. In their undifferentiated state, SH-SY5Y cells exhibit continuous proliferation and a non-polarized phenotype given by the absence of mature neuronal markers. In contrast, differentiated cells display a reduced proliferative rate, increased activity of neuron-specific enolase (NSE), and the presence of characteristic neuronal markers⁷². Consequently, SH-SY5Y cell lines are considered a valuable tool in neuroscience, facilitating investigations into neurodegeneration, cellular adaptation, responses to toxic substances, and potential protective measures. These cell lines have been crucial in studying Parkinson's disease, Alzheimer's disease, and viral infections.

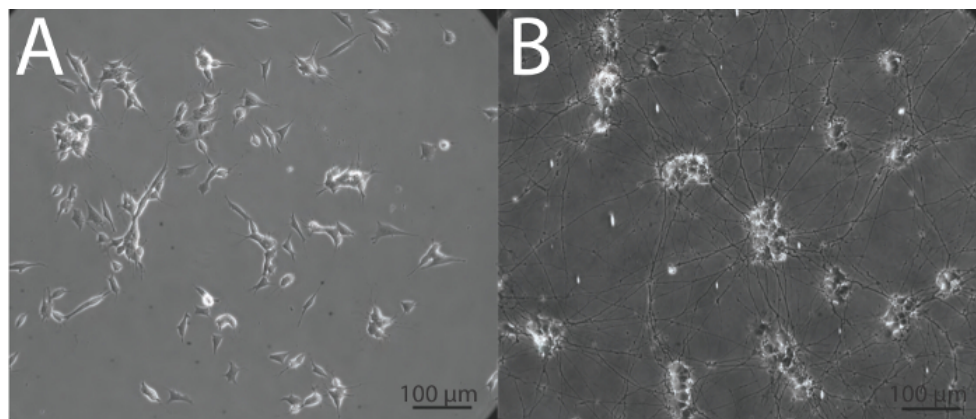


Figure 2.4: Morphological appearance of (A) undifferentiated and (B) differentiated SH-SY5Y cells. Retrieved from Shipley, M, et al. (2016)⁷⁴.

2.7 State of the Art

Hydroxyapatite, a biocompatible bioactive ceramic, finds extensive use in biomaterials and biomedical applications. Adding samarium ions imparts antibacterial and luminescent properties, rendering samarium-doped hydroxyapatite (Sm:HAp) a focal point in numerous research studies.

In previous investigations, fluorescent Sm:HAp nanoparticles were successfully synthesized using a modified

sol-gel technique focusing on bio-imaging applications. The doped samples exhibited heightened green and red fluorescence intensity compared to undoped HAp. Biocompatibility assessments conducted on HeLa cell lines revealed efficient cellular uptake and reduced toxicity at lower doping concentrations. As a result, the combination of enhanced luminescence and favorable biocompatibility positions Sm:HAp as a promising in vitro imaging agent⁷⁵. Moreover, Sm:HAp was also tested on both human gingival fibroblast and hFOB 1.19 osteoblast cells, demonstrating proliferative capacity, increase in viability, and no disturbance in the cell's behavior^{6,7}. This suggests potential applications in bone and dental contexts.

Sm:HAp has been extensively investigated as a potential coating for implants, primarily attributed to its antimicrobial properties. Implant failure often stems from bacterial adherence and biofilm formation, leading to infections. Turcule et al., Iconaru et al., and Ciobanu et al. successfully developed antifungal Sm:HAp films on titanium or silicon substrates using sol-gel spin coating and thermal evaporation techniques. These techniques resulted in homogeneous and uniform films, effectively hindering the proliferation of *Candida albicans* ATCC 10231 fungal strain. Notably, higher concentrations of Sm exhibited greater antifungal activity^{1,2,76}. Additionally, the antimicrobial properties were evaluated against Gram-negative bacteria (*Pseudomonas aeruginosa* and *Escherichia coli*) and Gram-positive bacteria (*Enterococcus faecalis* and *Staphylococcus aureus*)^{3,6,7}.

Incorporating other chemical elements into Sm:HAp through co-doping can induce alterations in both the structure and performance of the samples. The introduction of Sr into SmHAp adjusts its luminescent properties, enabling control over fluorescence lifetime and characteristics by manipulating Sr concentration. This makes it suitable for potential applications in biomedicine, particularly in areas such as bio-imaging and bio-detection⁷⁷. Conversely, the La³⁺-doped Sm:HAp complex exhibits increased photocatalytic performance, attributed to its broader absorption range under visible light. The photocatalytic activity was evaluated using phenol degradation and suggests potential applications in both medical and environmental contexts⁷⁸. In conclusion, current studies focused on samarium-doped hydroxyapatite display diverse applications, particularly in the field of nanomedicine.

2.8 Characterization Techniques

2.8.1 Fourier Transform Infrared Spectroscopy

Fourier-Transform Infrared Spectroscopy (FTIR) is a vibrational spectroscopic technique used for qualitative and quantitative structural analysis across a wide range of materials at the molecular level⁷⁹. This technique relies on the interaction between infrared (IR) radiation and matter, enabling the characterization of atomic bonding structure by measuring the frequencies at which the substance absorbs radiation, resulting in molecular vibration. These fundamental vibrations produce distinctive absorption bands that can be associated with specific functional groups⁸⁰ and chemical bonds⁷⁹. Consequently, FTIR provides direct information about the functional groups, types of bonding, and molecular conformation present in a sample^{79,81}.

A molecule absorbs the incident infrared light when follows a certain selection rule. For a vibrational mode to be considered IR active, there must be a change in the electric dipole moment^{79,82}. The vibrational mode of a molecule can involve stretching (ν , symmetrical < asymmetrical), or bending or deformation⁸⁰ (δ , in plane and out plane)⁸².

The Fourier transform spectrophotometer (Figure 2.5) captures the IR spectrum, comprising a moving mirror, fixed mirror, beam splitter, IR radiation, and detector. In this system, the detector records the interferogram signal in energy versus time, simultaneously capturing all frequencies⁸³. Subsequently, the interferogram undergoes Fourier transformation to generate the final spectrum. The IR spectrum is situated in the mid-IR region, specifically ranging from 2.5 to 15 μm . In this region, transition energies correspond to changes in the vibrational energy state for various functional groups, covering from 4000 to 400 cm^{-1} . In general, single, double, and triple bonds are detected in specific wavenumbers, along with complex patterns of vibrations that are characteristic of the molecule⁸³. As a consequence, the vibrational frequencies of a particular chemical group are found in specific regions, determined by the types of atoms and chemical bonds present. Tables are accessible to facilitate the interpretation and assessment of the primary chemical groups⁸².

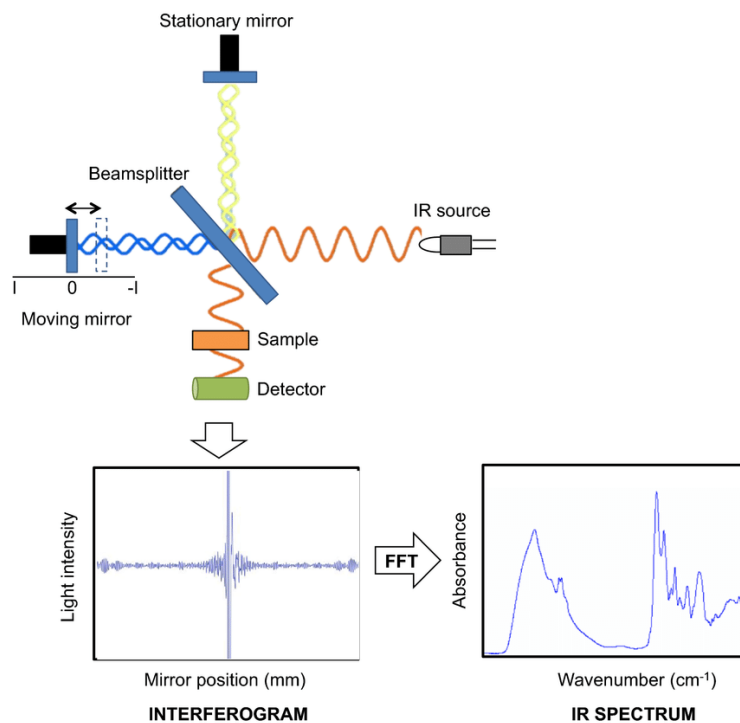


Figure 2.5: Basic component in Fourier transform infrared spectrometer. Retrieved from Campanella, B, et al. (2021)⁸⁴.

2.8.2 Raman Spectroscopy

Raman spectroscopy is a spectroscopic technique used to analyze vibrational, rotational, and other low-frequency modes within a given system⁸⁵. This technique studies the Raman scattering phenomenon which results from the interaction between photon and matter⁸⁶, leading to a shift in the frequency of the emitted photon and inducing molecular vibration⁸⁴. This wavelength shift of the scattered light depends upon the chemical composition of the molecules responsible for the scattering process. Consequently, the Raman spectrum is registered in the visible or near IR region⁸⁴ and serves as a characteristic fingerprint for compounds, enabling the identification of various samples⁸⁷ based on their molecular structure.

Inelastic or Raman scattering arises from the distortion of the electron cloud around the nuclei during vibration. This alteration of polarizability forms a short-lived state known as a virtual state, which is unstable, leading to the instantaneous re-radiation of the photon⁸⁶. This interaction occurs within a brief period of approximately 10^{-15} seconds⁸⁴. This type of scattering involves the transfer of energy to the scattered photon, resulting in either lower energy (Stokes) or higher energy (Anti-Stokes) compared to the absorbed photon, as observed in Figure 2.6. This depends on whether the vibration is associated with a transition to an excited or lower vibrational state. Furthermore, Raman scattering is intrinsically a weak process, with only one in every $10^6 - 10^8$ scattered photons experiencing inelastic scattering⁸⁶.

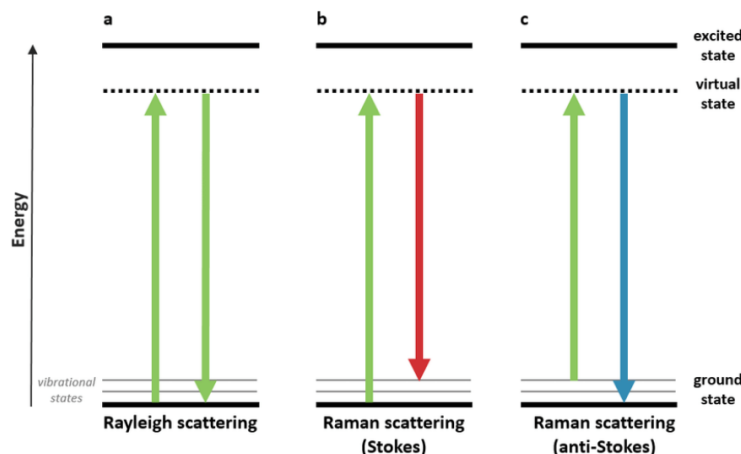


Figure 2.6: Diagram of Rayleigh and Raman scattering processes: a) Rayleigh scattering, b) Raman Stokes scattering and c) Raman anti-Stokes scattering. Retrieved from Moura, C, et al. (2016)⁸⁸.

A conventional Raman spectrometer comprises some major components, including an excitation source (UV, visible, or near-IR), collection optics, a monochromator or an interferometer, and a detector⁸⁴. Indeed, Raman and IR spectroscopies are regarded as complementary techniques. Both methods analyze the vibrational modes of molecules, capturing transitions that may be absent or weak in one spectrum but are evident in the other. Typically,

Raman spectroscopy is more adept at detecting symmetrical or in-phase vibrations and non-polar groups, whereas IR spectroscopy excels in observing asymmetric or out-of-phase vibrations and polar groups. The application of group theory is common in predicting which vibrations will be active.

2.8.3 X-Ray Diffraction

X-ray diffraction (XRD) is a non-destructive characterization technique that provides detailed information about the crystallographic structure, phases, orientation, and parameters⁸⁹ of a wide range of materials, including powder, solids, and liquids. XRD is based on the constructive interference of elastic scattered monochromatic x-rays by atoms from different lattice planes in a crystalline sample. XRD relies on the satisfaction of Bragg's law (eq. 2.1), which relates the wavelength of electromagnetic radiation (λ) to the diffraction angle (θ) and the lattice spacing (d)⁹⁰.

$$n\lambda = 2d \sin \theta \quad (2.1)$$

An x-ray diffractometer (Figure 2.7) mainly consists on an x-ray tube, a sample holder, and an x-ray detector⁸⁹. The diffractometer adjusts the diffraction angle by moving the x-ray tube, sample, or detector. During this process, diffraction spacing and intensities are recorded, forming a diffractogram⁹¹. Since the d-spacing values are distinctive for each compound, identifying an unknown substance involves comparing these values and relative intensities with standard reference patterns in the Powder Diffraction File (PDF). This file is updated annually by the International Centre for Diffraction Data (ICDD)⁹². Consequently, the resulting XRD pattern comprises diffraction peaks corresponding to specific crystallographic planes within the material, serving as a unique and characteristic fingerprint.

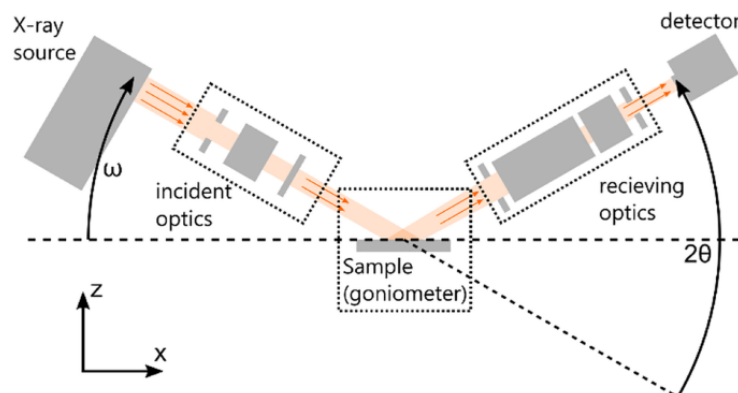


Figure 2.7: Schematic of the experimental principle for X-ray diffraction. Retrieved from Harrington, G, et al. (2021)⁹³.

2.8.4 Photoluminescence Spectroscopy

Photoluminescence (PL) spectroscopy is an optical characterization technique that relies on photo-excitation and PL processes to explore the electronic structure of materials. When light radiates a sample, electrons undergo excitation from equilibrium to excited electronic states, subsequently emitting photons during relaxation. Electronic band transitions are quantized, and the excess energy can be released through either radiative (electromagnetic radiation, i.e., photons) or non-radiative (heat, i.e., phonons) transitions^{94,95}. PL spectroscopy specifically focuses on transitions from the excited to ground state, depicted in the excitation spectrum as intensity versus excitation wavelength⁹⁵. Furthermore, it is a non-destructive and contactless method, facilitating bandgap determination, impurity level detection, defect analysis⁹⁶, and examination of recombination mechanisms. The essential components of PL spectroscopy equipment typically include a light source, monochromator, collection optics, and detector⁹⁷. The light source can be any with energy surpassing the material's band gap, ensuring adequate power for excitation and signal generation⁹⁴.

2.8.5 Scanning Electron Microscopy

Scanning electron microscopy (SEM) is a specialized electron microscopy technique that employs a focused electron beam to generate detailed images of samples at the nanometer to micrometer scale⁹⁸. The electron beam systematically scans the sample's surface, and the emitted electrons contribute to the formation of the image. SEM offers magnifications from approximately 10 times to 300,000 times⁹⁸, surpassing the capabilities of traditional microscopes. Through the interaction between atoms of the sample and electrons, SEM provides valuable information regarding surface topography, comprising factors such as morphology, surface texture, particle size, and distribution. Additionally, SEM facilitates insights into the chemical composition of the specimen^{98,99}.

SEM comprises main elements such as: an electron gun as the source, electromagnetic lenses (condenser and objective) for beam control, apertures and a column for electron passage, a specimen chamber with position and orientation controls, and an electron detector capturing backscattered and secondary electrons. The entire system operates within a high vacuum¹⁰⁰. SEM image production involves the utilization of both secondary electrons (SE) and backscattered electrons (BSE).

SEs are electrons with low energy ($E_{SE} < 50$ eV) that originate from the surface and near-surface regions of a specimen due to inelastic scattering when the sample is bombarded with primary electrons (PE) from the high-energy beam. Accordingly, SEs mainly offer topographic information¹⁰¹. Conversely, backscattered electrons (BSEs) possess a significant portion of the energy of PEs¹⁰². Due to their high energy, BSEs originate from deeper subsurface layers of the specimen when compared to SEs¹⁰³, as illustrated in Figure 2.8. BSEs result from elastic scattering interactions between PEs and the nuclei of sample atoms, causing trajectory deviation before returning to the sample surface^{99,102}, and maintaining their high energy. BSEs can arise from single deflections ($> 90^\circ$) induced by Coulombic forces or multiple low-angle deflections that collectively constitute a large-angle deflection¹⁰⁴. Significantly, BSEs provide valuable information about the chemical composition of materials through

atomic number contrast. Specifically, heavier elements can cause more pronounced deflections of incident electrons, leading to brighter contrast in SEM images.

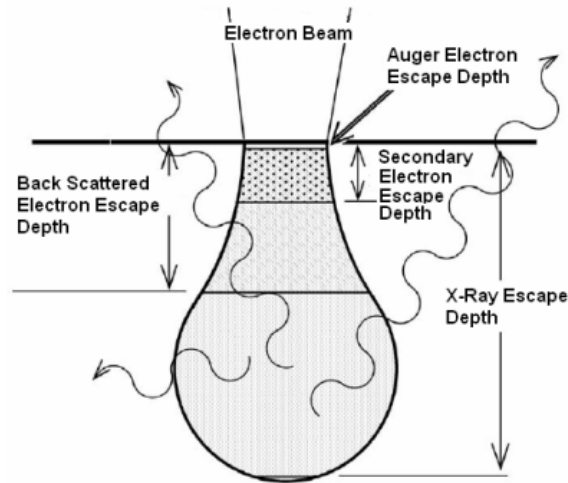


Figure 2.8: Electron - matter interaction volume and types of signal generated. Retrieved from Hafner, B (2007)¹⁰⁰.

Energy Dispersive X-ray Spectroscopy (EDS) is used in SEM for elemental analysis, relying on the interaction between atoms in the sample and incident PEs to measure the energy and intensity distribution of emitted x-rays, which are characteristic of specific elements¹⁰⁵. The emission of characteristic X-rays occurs when an outer shell electron fills a vacancy in the inner shell, created by the ejection of an inner shell electron through excitation induced by the PE beam¹⁰⁶. The energy of these X-rays corresponds to the difference in energy between the two shells, revealing the atomic structure and providing information on the chemical composition of the specimen. Additionally, the intensity of the X-rays offers insights into the relative concentration of elements in the sample⁹⁸. Hence, the combination of SEM and EDS enables both qualitative and semi-quantitative analysis.

Chapter 3

Methodology

3.1 Synthesis of the Biomaterial

3.1.1 Reagents

The samples were synthesized via wet methods. For this, the HAp precursors were supplied by Sigma-Aldrich (St. Louis, Missouri, United States), including calcium chloride (CaCl_2 , ACS reagent, $\geq 99\%$), diammonium hydrogen phosphate ($(\text{NH}_4)_2\text{HPO}_4$, reagent grade, $\geq 98\%$), and ammonium hydroxide ($(\text{NH}_4)\text{OH}$). Additionally, Sm^{3+} ions for doping come from samarium(III) nitrate hexahydrate ($\text{Sm}(\text{NO}_3)_3 \cdot 6\text{H}_2\text{O}$) with a purity of 99.9% trace metals basis.

3.1.2 Hydroxyapatite (HAp) and Samarium Doped Hydroxyapatite (Sm:HAp)

Hydroxyapatite was synthesized by hydrothermal method (Figure 3.1) with calcium to phosphate ratio fixed to 1.67, $\text{Ca}/\text{P} = 1.67$. For the synthesis, $(\text{NH}_4)_2\text{HPO}_4$ was dissolved in 25 mL distilled water. A 25 mL of CaCl_2 solution at 10 mmol was added dropwise from a burette to the $(\text{NH}_4)_2\text{HPO}_4$ solution in constant agitation at room temperature. After that, 5 mL of $(\text{NH}_4)\text{OH}$ was added to the resulting solution to increase the pH from 5 to 10. Then, it was mounted in a reactor and placed on the stove at 125 °C for 24 hours. The sample is washed with distilled water until the pH drops to 7. Next, it was dried on the stove at 60 °C for 48 hours and comprised into pellets. Finally, the sample is calcinated at 200 °C, 400 °C, 600 °C, and 800 °C.

Similarly, samarium doped hydroxyapatite nanoparticles with the chemical formula $\text{Ca}_{10-x}\text{Sm}_x(\text{PO}_4)_6(\text{OH})_2$, $x_{\text{Sm}} = (0.05, 0.10, 0.50, 1.00)$ were synthesized by the hydrothermal method with $(\text{Ca} + \text{Sm})/\text{P}$ fixed to 1.67. Here, $\text{Sm}(\text{NO}_3)_3 \cdot 6\text{H}_2\text{O}$ was dissolved with CaCl_2 solution. The concentrations and masses of the compounds are described in Table 3.1.

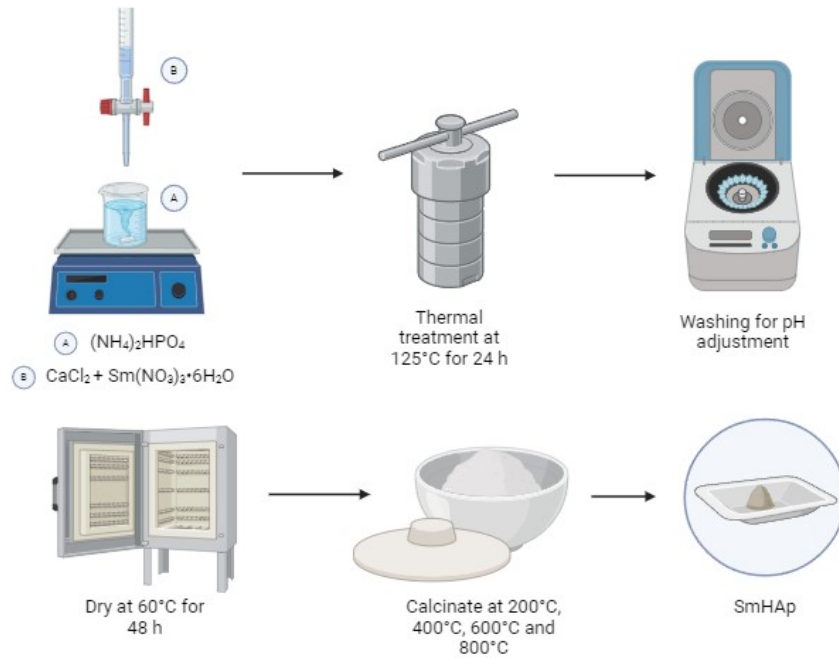


Figure 3.1: Hydrothermal synthesis method of Sm:HAp samples.

Table 3.1: Concentration and masses of the compounds following the fixed $(\text{Ca}+\text{Sm})/\text{P} = 1.67$.

$c_{\text{Ca}^{2+}}$ (mmol)	$c_{\text{Sm}^{3+}}$ (mmol)	$c_{(\text{PO}_4)^{3-}}$ (mmol)	$m_{\text{Ca}^{2+}}$ (g)	$m_{\text{Sm}^{3+}}$ (g)	$m_{(\text{PO}_4)^{3-}}$ (g)
10.00	0.00	5.98	1.1098	0.0000	0.7898
9.95	0.05	5.98	1.1042	0.0222	0.7898
9.90	0.10	5.98	1.0987	0.0444	0.7898
9.50	0.50	5.98	1.0543	0.2222	0.7898
9.00	1.00	5.98	0.9988	0.4445	0.7898

3.2 Characterization

The structure of samarium-doped hydroxyapatite was studied using Fourier-transform infrared spectroscopy (FTIR), Raman spectroscopy, and X-ray diffraction (XRD). Morphological features were analyzed via scanning electron microscopy (SEM), while optical properties were examined using photoluminescence spectroscopy.

3.2.1 Fourier Transform Infrared Spectroscopy

FTIR spectroscopy was used to analyze the changes of the functional groups in the structures of samarium doped hydroxyapatite. The characterization was conducted using the Cary 630 FTIR spectrometer with the Diamond ATR accessory (Agilent Technologies, Inc., Santa Clara, United States). The samples were analyzed in the range of 450 - 4000 cm^{-1} at room temperature.

3.2.2 Raman Spectroscopy

Raman Spectroscopy was employed to analyze the vibrational modes of the samples. The LabRAM HR Evolution Confocal Raman Microscope (HORIBA France SAS, Longjumeau, France) was utilized to obtain the spectra. The Raman analysis was conducted with acquisition times of 5 s, covering the range of 0 to 3500 cm^{-1} . Excitation of the samples was achieved using a 633 nm He-Ne laser.

3.2.3 X-Ray Diffraction

The crystalline structure of the Sm:HAp powders was identified by X-ray diffraction using a MiniFlex benchtop X-ray diffractometer (Rigaku Corporation, Tokyo, Japan), with monochromatic $\text{CuK}\alpha$ radiation ($\lambda = 1.5418 \text{ \AA}$). The diffraction patterns were collected in the 2θ range between 10° and 70° , with a step of 0.01° and 10 s measuring time per step.

3.2.4 Scanning Electron Microscopy

Surface morphology was investigated using SEM, for both uncalcined and calcined samples at 800°C . The samples included pure HAp and Sm:HAp at $x_{Sm} = 0.05$ and 0.5 . Before analysis, the samples were dispersed in a water/ethanol solution. SEM imaging was conducted using the MIRA 3 equipment (TESCAN, Brno, Czechia), a field-emission scanning electron microscope (FE-SEM). The images were acquired in the backscattered electron (BSE) mode with an acceleration voltage of 10 kV and a working distance of 9.95 nm. Micrographs were displayed at 16.7 kx and 83.3 kx magnifications. EDS is incorporated into the SEM to acquire elemental and compositional information from the samples. The Quantax system (Bruker Nano GmbH, Berlin, Germany) was utilized for EDS microanalysis in the SEM.

3.2.5 Photoluminescence Spectroscopy

Photoluminescence (PL) experiments were conducted at room temperature, utilizing an optical table setup that included a stable 405 nm diode laser for sample excitation, two mirrors, a sample holder, the MicroHR Short Focal Length Imaging Spectrometer (Horiba, Ltd., Kyoto, Japan), and the DSS-SIGA020 In/Ga/Ar Solid State Detector (Horiba, Ltd., Kyoto, Japan). The analysis was performed within the wavelength range of 500 to 800 nm, and an integration time of 0.01 s.

3.3 Cytotoxicity Study

3.3.1 Reagents

Essential components for cell culture and maintenance were supplied by Gibco, a division of Thermo Fisher Scientific (Waltham, Massachusetts, United States). These included Dulbecco's Modified Eagle Medium (DMEM), fetal bovine serum (FBS), penicillin-streptomycin antibiotic, phosphate-buffered saline solution (PBS), and 0.25% trypsin-EDTA. Additionally, Gibco also supplied the 0.4% trypan blue solution for Trypan Blue technique, and Cell Proliferation Kit I from Roche (Basel, Switzerland) was utilized for MTT assays.

3.3.2 Procedure

DMEM Medium Preparation

DMEM is a widely used cell culture medium for the growth and sustenance of various cell lines, including SH-SY5Y. A 1x dilution, DMEM culture medium with constituents as 4.5 g/L D-glucose, L-glutamine, and 110 mg/L sodium pyruvate is complemented with 10% (v/v) FBS and 1% (v/v) penicillin-streptomycin antibiotic to prevent bacterial and fungal contamination. Subsequently, the medium is filtered using a PES membrane disposable filter with a pore size of 0.22 μm . The resulting culture medium is then stored at 4°C for maintenance purposes.

SH-SY5Y Cell Culture Maintenance

Regular maintenance is essential for ensuring optimal cell health and growth. Cells are cultured by thawing a vial of frozen SH-SY5Y cells from a liquid nitrogen tank and then transferred to a T-25 cell culture flask filled with 5 mL of complete DMEM medium. The flask is placed inside a CO₂ incubator, set at 37°C with 5% CO₂. Ongoing cell growth is systematically observed using the Motic AE31E inverted microscope (Motic China Group Co., Hong Kong, China). The culture medium is refreshed every 2-3 days with fresh medium to supply essential nutrients and eliminate waste byproducts. Generally, the medium is replaced upon observing a change in color, indicating a pH shift associated with the metabolic activity of the cells and nutrient availability.

Passaging is carried out when cells reach approximately 80% confluence. For cell passage, the medium is retired from the flask. Cells undergo a wash with 2-3 mL of filtered PBS and are then detached using 5 mL trypsin. After a 5-min incubation period, 3 mL of culture medium is introduced to neutralize trypsin and prevent cell damage. Following, cells are centrifuged at 5000 rpm for 5 minutes. The supernatant is discarded, and the pellet is resuspended in 2-3 mL of culture medium. Cell counting is performed using a Neubauer chamber to determine the required quantity for subsequent experiments.

Treatment Preparation

The treatments are prepared using a sterile sodium chloride saline solution. A 10 mg/L dilution was created for each Sm:HAp sample and subsequently homogenized in an ultrasonic bath. The resulting solution is then further diluted

into the culture medium within sterile 48-well and 96-well microplates, with 4 repetitions each.

Trypan Blue

The trypan blue assay is a widely utilized research technique for evaluating cell viability, distinguishing between live and dead cells in cell culture by staining the dead ones. In this experiment, cells were cultured at a concentration of 5000 cells per well in a 48-well plate, with each well containing 400 μL of culture medium. Following a 48-hour incubation, 10 μL of treatments and 40 μL of DMSO were added as illustrated in Figure A.1. The trypan blue technique (Figure 3.2) is performed 24 hours post-treatment. In this step, 400 μL of a 0.4% trypan blue solution was applied to each well, followed by a 10-minute incubation at room temperature. The well contents were discarded, and cells were observed using an inverted microscope for cell counting.

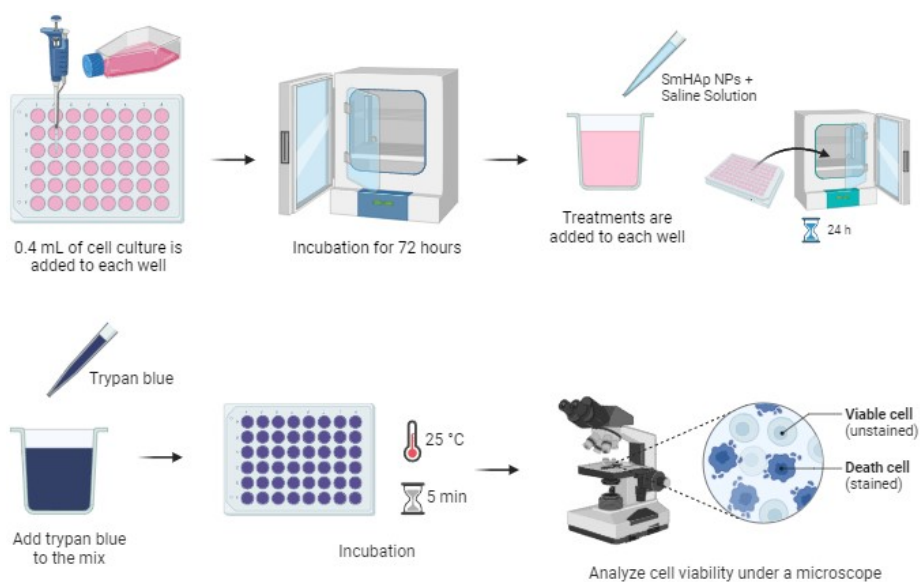


Figure 3.2: Trypan Blue Exclusion Test Protocol.

MTT Assay

The MTT assay, a colorimetric method for evaluating cell viability and proliferation, relies on converting a yellow tetrazolium salt into purple formazan crystals by metabolically active cells. In this study, cells were cultured at a concentration of 5000 cells per well in a 96-well plate, with each well containing 100 μL of culture medium. After a 48-hour incubation, 10 μL of treatments and 10 μL of DMSO were added, as depicted in Figure A.1. Similarly, the MTT assay (Figure 3.3) was conducted 24 hours post-treatment, adding 10 μL of MTT labeling reagent to each well, followed by a 4-hour incubation. Afterward, 100 μL of solubilization buffer was introduced to each well. After a

12-hour incubation, absorbance was measured at a 630 nm wavelength using the Rayto RT-2100C microplate reader spectrophotometer (Rayto Life and Analytical Sciences Co., Ltd, Shenzhen, China).

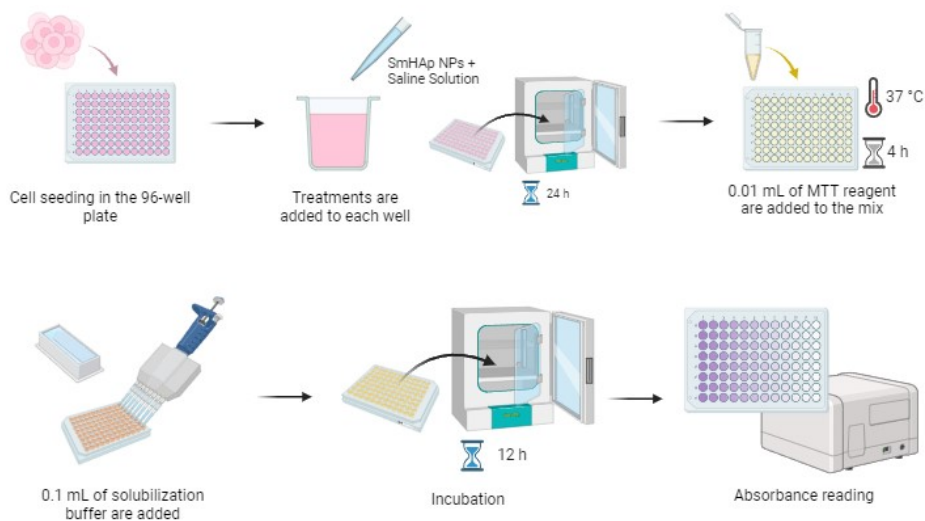


Figure 3.3: MTT Assay Protocol.

Data Analysis

The data were presented as the mean value \pm standard deviation (SD). For the analysis of trypan blue data, the counted cells were processed to determine the percentage of viable cells using the following expression:

$$\% \text{ of viable cells / mL} = \frac{\text{Total number of viable cells}}{\text{Total number of cells}} * 100 \quad (3.1)$$

To analyze absorbance data derived from MTT assays, the real absorbance was determined by subtracting the absorbance of the blank (medium) from the spectrometer-measured absorbance. The resulting absorbance values were then converted into percentages based on the absorbance of the control (cells untreated with Sm:HAp). Consequently, the relative cell viability (%) is computed using the following equation:

$$\text{Relative Cell Viability (\%)} = \frac{[A]_{\text{treatment}}}{[A]_{\text{control}}} * 100 \quad (3.2)$$

Chapter 4

Results & Discussion

4.1 Structural Characterization

4.1.1 Fourier Transform Infrared Spectroscopy

FTIR measurements were conducted to examine the vibrational bands within the structures of samarium-doped hydroxyapatite, Sm:HAp ($\text{Ca}_{10-x}\text{Sm}_x(\text{PO}_4)_6(\text{OH})_2$ with $x_{Sm} = 0, 0.05, 0.1, 0.5,$ and 1.0), at various temperatures: room temperature, $200\text{ }^\circ\text{C}$, $400\text{ }^\circ\text{C}$, $600\text{ }^\circ\text{C}$, and $800\text{ }^\circ\text{C}$. In general, the FTIR spectra of the samples displayed the characteristic vibrational modes of pure hydroxyapatite, corresponding to hydroxyl (OH^-), phosphate (PO_4^{3-}), and absorbed water (H_2O).

Figure 4.1 presents the FTIR spectra of Sm:HAp at varying samarium concentrations under room temperature conditions. As reported in the literature, the bands centered around 630 cm^{-1} and 3570 cm^{-1} correspond to the librational (ν_L) and stretching (ν_s) vibrational modes of hydroxyl, respectively¹⁰⁷. The presence of these bands suggests a well-crystallized structure⁴². The vibrations associated with the phosphate group are: the peaks at approximately 1020 cm^{-1} and 1088 cm^{-1} attributed to the triply degenerated asymmetric stretching vibration (ν_3) of the P-O bond; the shoulder at 961 cm^{-1} assigned to the non-degenerated symmetric stretching vibration (ν_1) of the P-O bond; the peaks at 560 cm^{-1} and 600 cm^{-1} designated to the triply degenerated bending mode (ν_4) of the O-P-O bond; and a weak peak at $\sim 473\text{ cm}^{-1}$ ascribed to the double degenerated bending mode (ν_2)¹⁰⁸. The vibrational peak at 1626 cm^{-1} corresponds to the H-O-H bending mode of lattice water, as well as the region between $3000\text{-}3600\text{ cm}^{-1}$ ^{4,7,107}, observed at $x_{Sm} = 1.0$. At this concentration, a band at 1425 cm^{-1} emerges, indicating C-O vibration (ν_3), characteristic of the carbonate group (CO_3^{2-}). Bands specific to the hydrogen phosphate group (HPO_4^{2-}) are found at around 870 cm^{-1} ¹⁰⁸. An additional peak for (HPO_4^{2-}) is identified at $\sim 533\text{ cm}^{-1}$ for $x_{Sm} = 1.0$ ¹⁰⁷.

As observed in Figure 4.1, the regions corresponding to the bands at $1088, 960, 872, 630,$ and 475 cm^{-1} exhibit a diminishing contribution when increasing the concentration of samarium in the samples. When $x_{Sm} = 1.0$, these

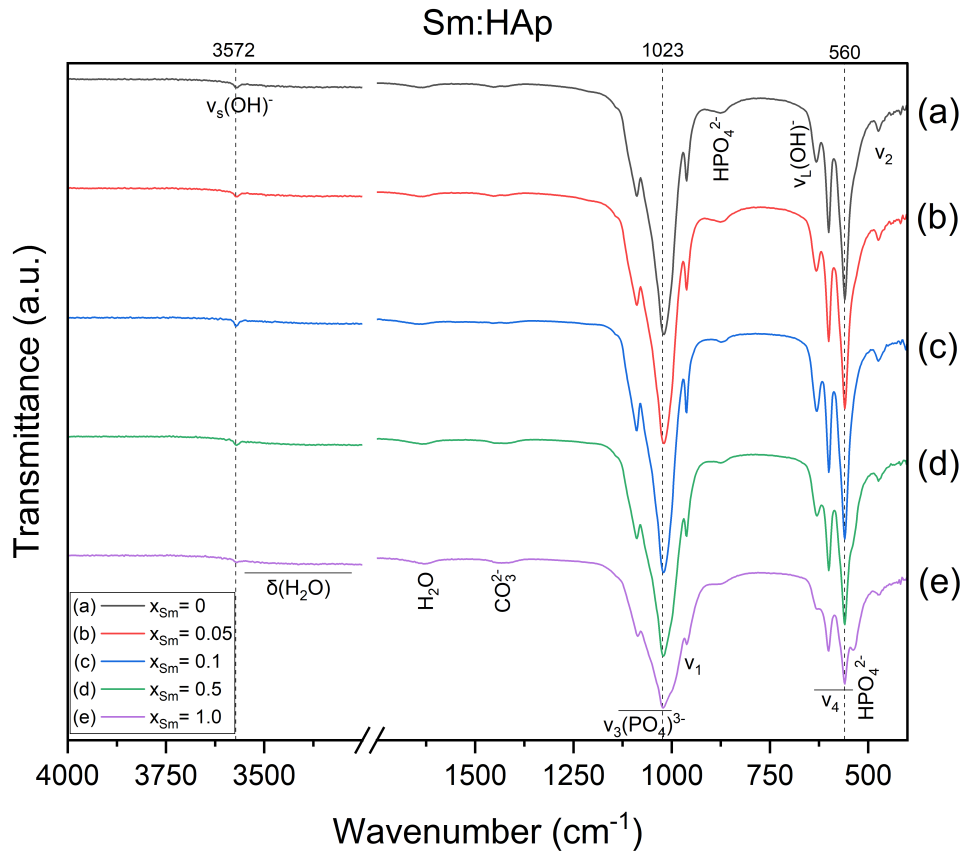


Figure 4.1: FTIR spectra of Sm:HAp at different samarium concentrations ($x_{Sm} = 0, 0.05, 0.1, 0.5, 1.0$).

bands are almost absent. The disappearance and shifts of these peaks may be attributed to the introduction of Sm^{3+} ions. The increasing concentration of samarium may induce structural changes in the HAp, affecting the local environment within the crystal lattice and the vibrational properties of specific regions. Similar behavior is evident in Sm:HAp samples calcined at 200 °C, 400 °C, 600 °C, and 800 °C, as illustrated in Figure 4.2. However, the $\nu_3(\text{CO}_3)^{2-}$ band at 1425 cm^{-1} disappears from 400 °C onward, and the lattice water band at 1626 cm^{-1} vanishes at 600 °C. This phenomenon may be attributed to a gradual decomposition or release of entrapped species during the heating process. At 800 °C, the $(\text{HPO}_4)^{2-}$ peaks disappear completely. In addition, changes in the peak shapes corresponding to the phosphate group are observed in these samples. They resemble the peak shape of β -tricalcium phosphate (β -TCP, $\beta\text{-Ca}_3(\text{PO}_4)_2$)¹⁰⁹, suggesting a partial phase change occurring at 800 °C for $x_{Sm} = 0.05, 0.5, 1.0$.

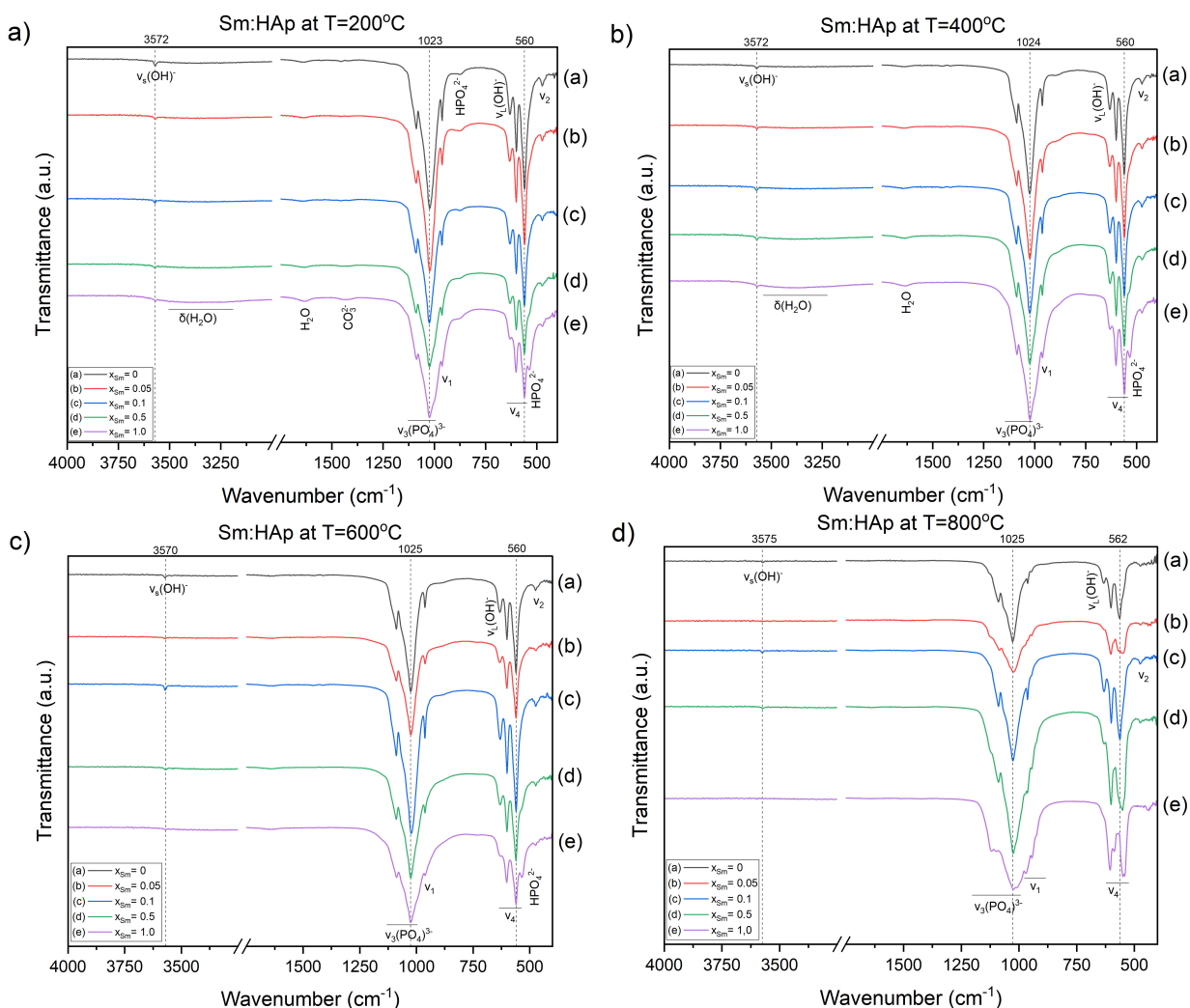


Figure 4.2: FTIR spectra of Sm:HAp at different samarium concentrations ($x_{Sm} = 0, 0.05, 0.1, 0.5, 1.0$) for different calcination temperatures: (a) 200 °C, (b) 400 °C, (c) 600 °C, and (d) 800 °C.

4.1.2 Raman Spectroscopy

Raman spectroscopy was employed to complement the FTIR spectroscopy analysis for the different Sm:HAp samples. This technique offers valuable information due to its sensitivity to fine structural variations, allowing for the detection of chemical transformations from HAp to either β -TCP or biphasic tricalcium phosphate (BCP)¹¹⁰. The primary vibrational bands observed were assigned to the characteristic modes of the tetragonal phosphate group (PO_4)³⁻ of crystalline HAp.

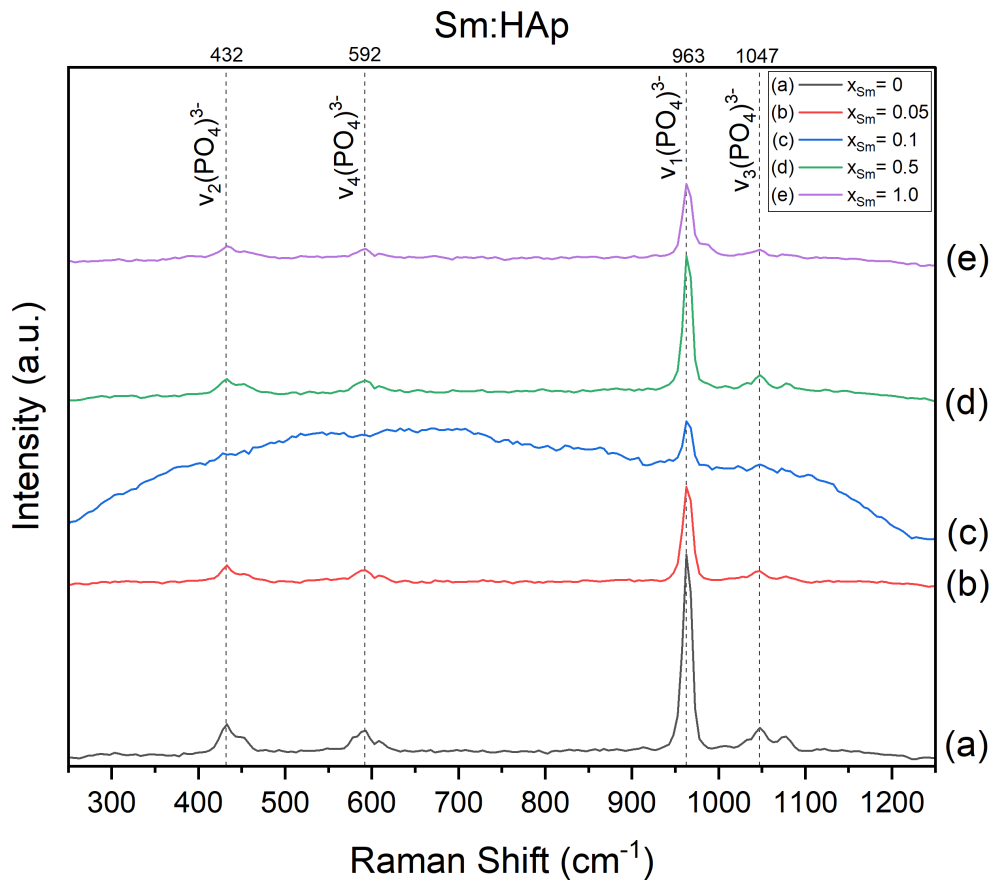


Figure 4.3: Raman spectra of Sm:HAp at different samarium concentrations ($x_{Sm} = 0, 0.05, 0.1, 0.5, 1.0$).

Figure 4.3 illustrates the Raman spectra in the 250 – 1250 cm^{-1} region, with the corresponding experimental band positions and assignments. The most prominent band, observed at 962 cm^{-1} , is attributed to the ν_1 symmetric stretching vibrational mode of the P-O bond in $(\text{PO}_4)^{3-}$. Nearby, peaks at 1047 and 1077 cm^{-1} correspond to the ν_3 asymmetric stretching mode of the P-O bond. At lower wavenumbers, the 430-452 cm^{-1} range and the 592-607 cm^{-1} range are associated with the ν_2 and ν_4 bending vibrations of O-P-O, respectively^{111–113}. Literature reports that ν_1 peaks in the 962-964 cm^{-1} range indicates a highly crystalline HAp¹¹⁴. Moreover, the intensity of the vibrational bands decreases as the concentration of samarium increases. The substitution of Ca^{2+} with Sm^{3+} ions may introduce disorder, leading to a reduction in the overall crystallinity of the material. This alteration affects the Raman scattering efficiency, resulting in decreased peak intensity. For $x_{Sm} = 0.1$, ν_2 , ν_3 , and ν_4 peaks may go unnoticed due to fluorescence background. This fluorescence may arise from electronic transitions within the sample, induced by the excitation of luminescent samarium ions at optimal concentration.

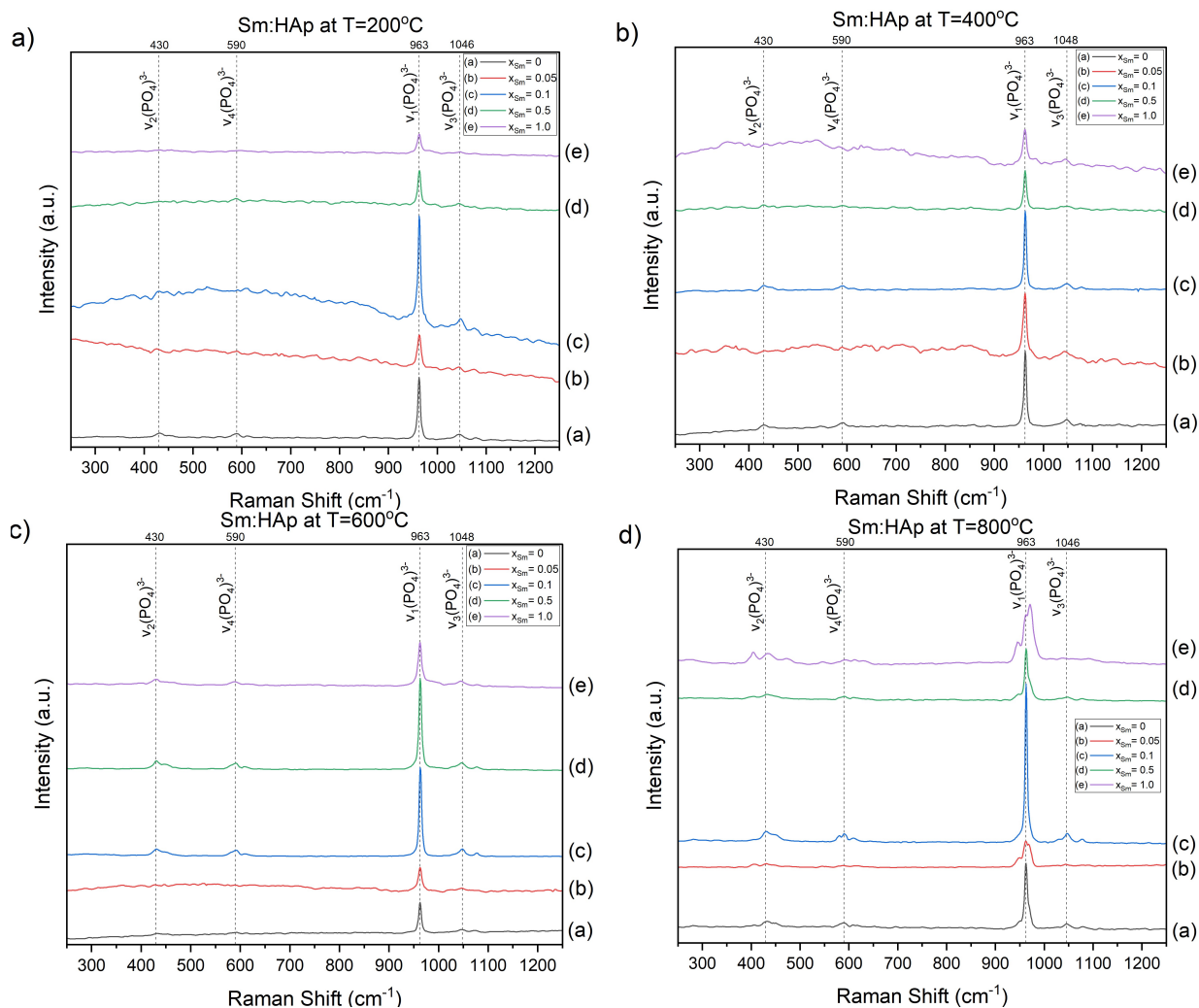


Figure 4.4: Raman spectra of Sm:HAp at different samarium concentrations ($x_{Sm} = 0, 0.05, 0.1, 0.5, 1.0$) for different calcination temperatures: (a) 200 °C, (b) 400 °C, (c) 600 °C, and (d) 800 °C.

Similar results are observed on samples calcined at 200 °C, 400 °C, 600 °C, and 800 °C, as depicted in Figure 4.4. Nonetheless, at certain dopant concentrations and calcination temperatures, specific bands at 430, 590, and 1048 cm^{-1} corresponding to ν_2 , ν_4 , and ν_3 , respectively, disappear. The absence of these bands may be associated with a decrease in crystallinity, alterations in crystal size, or changes in the local environment. Some samples also exhibit fluorescence, such as $x_{Sm} = 0.05$ at 200 °C, 400 °C, and 600 °C; $x_{Sm} = 0.1$ at 200 °C; and $x_{Sm} = 1.0$ at 600 °C. No noticeable peak shift is observed. At 800 °C, the peak shapes in the ν_1 region change due to the

presence of an additional peak at 971 cm^{-1} with high intensity in samples with $x_{Sm} = 0.05$ and 0.1 . According to the literature, a vibrational mode at $\sim 969\text{ cm}^{-1}$, accompanied by a wide band at $940\text{--}950\text{ cm}^{-1}$, corresponds to the β -TCP spectrum¹¹⁰. This suggests a partial conversion of HAp to β -TCP.

4.1.3 X-ray Diffraction

X-ray diffraction (XRD) analysis was conducted to identify the crystalline structure and phases of both HAp and Sm:HAp samples at varying calcination temperatures. In Figure 4.5, the XRD pattern of uncalcined Sm:HAp samples ($x_{Sm} = 0, 0.05, 0.1, 0.5, 1.0$) is presented. All diffraction peaks correspond to the hexagonal phase of pure hydroxyapatite with $P6_3/m$ spatial symmetry, as well as major characteristic peaks occurring at diffraction angles $25.8^\circ, 31.7^\circ, 32.8^\circ, 34.1^\circ, 39.7^\circ, 46.7^\circ, 49.4^\circ,$ and 53.1° ⁷⁷. These angles align with the crystal planes (002), (3-21), (300), (202), (4-30), (4-22), (3-23), and (004) from the standard pattern (COD Card: 00-900-2214) in the ICDD database. In addition, the diffraction data exhibits distinct and well-defined peaks, and no additional peaks suggestive of secondary phases or impurities were detected^{4,77}. These results demonstrate the substitution of Sm^{3+} ions for Ca^{2+} ions occurred successfully without altering the crystal structure of hydroxyapatite^{4,6}.

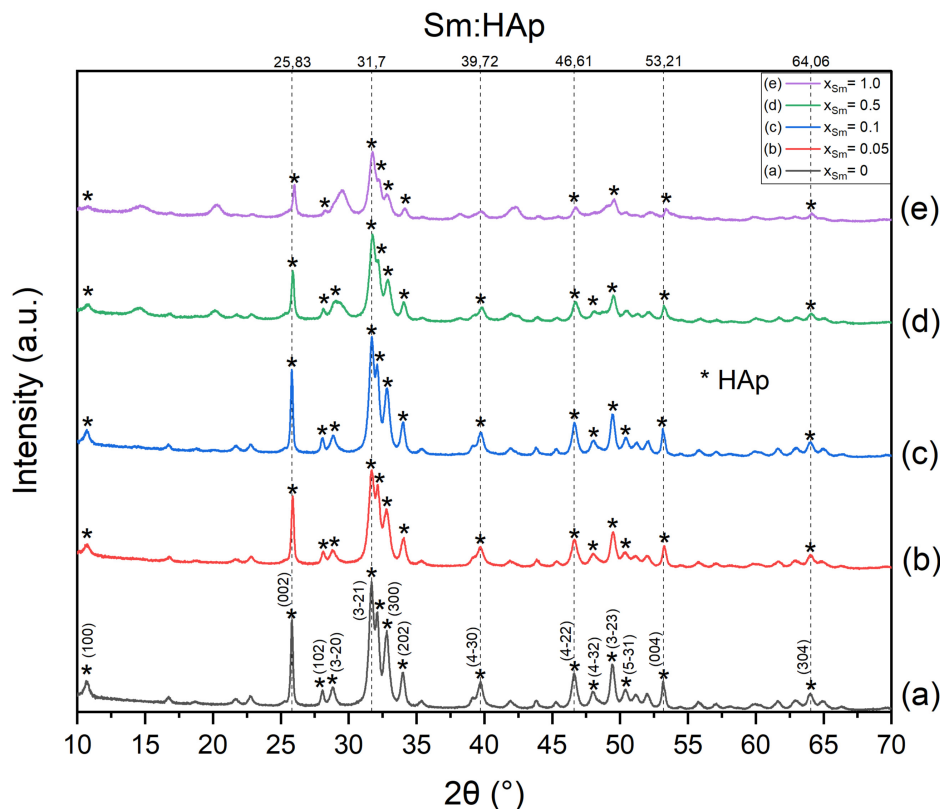


Figure 4.5: XRD pattern of Sm:HAp at different samarium concentrations ($x_{Sm} = 0, 0.05, 0.1, 0.5, 1.0$).

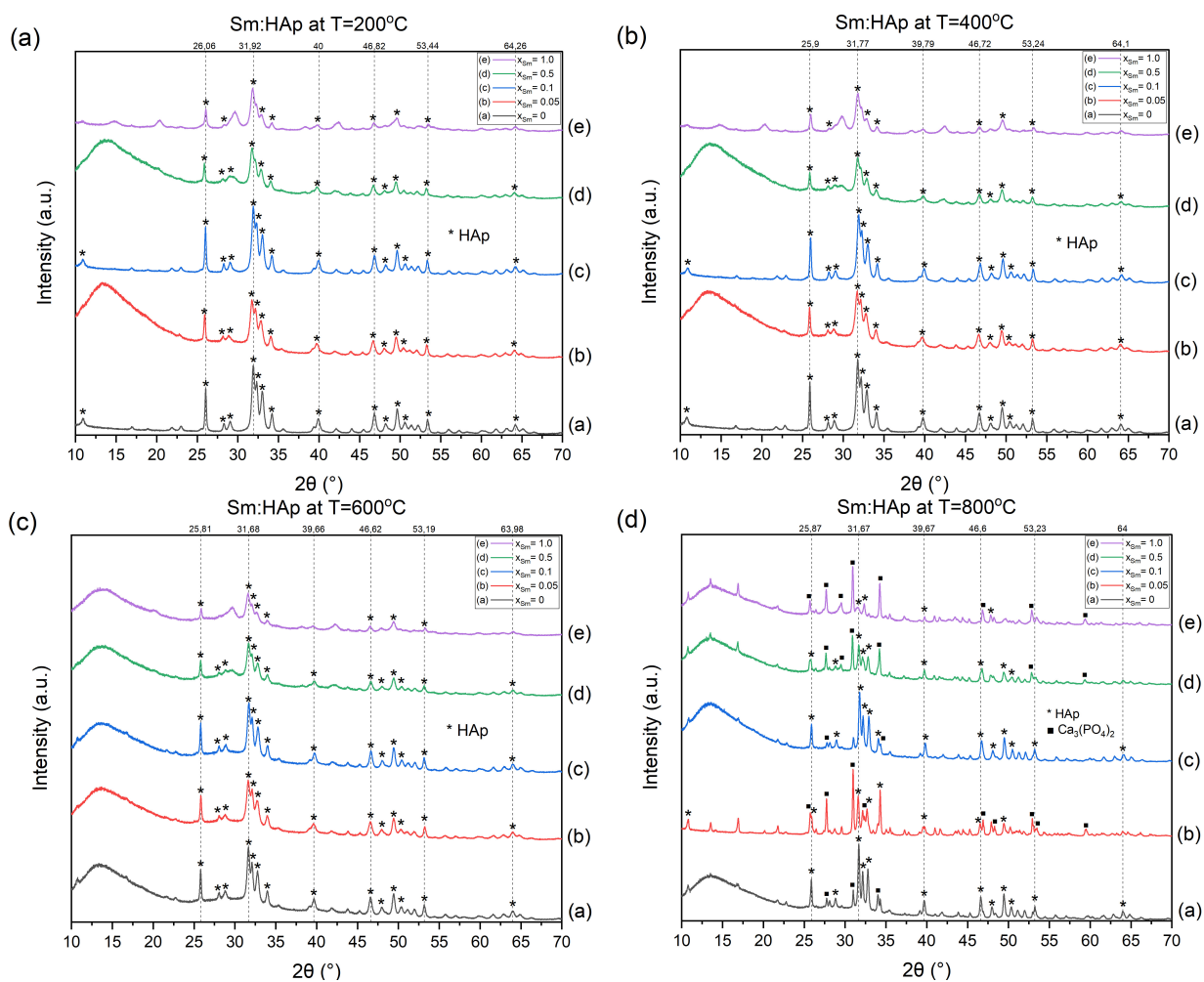


Figure 4.6: XRD pattern of Sm:HAp at different samarium concentrations ($x_{Sm} = 0, 0.05, 0.1, 0.5, 1.0$) for different calcination temperatures: (a) 200 °C, (b) 400 °C, (c) 600 °C, and (d) 800 °C.

As observed in Figure 4.5, the Sm:HAp samples maintain the characteristic hexagonal crystal structure and spatial symmetry of pure apatite. However, upon substituting Sm^{3+} for Ca^{2+} ions, the diffraction peaks exhibit an apparent shift towards larger angles, accompanied by peak broadening. This shift is attributed to the introduction of smaller Sm^{3+} ions ($r_{ion} = 1.079 \text{ \AA}$) compared to Ca^{2+} ions ($r_{ion} = 1.260 \text{ \AA}$), resulting in a contraction of the crystal spacing. Smaller ions typically lead to closer atomic packing, causing a decrease in interatomic distances and alterations in the angles between crystal planes. This decrease in interatomic distance is reflected in the XRD pattern as a shift towards larger 2θ angles, in agreement with Bragg's law. Accordingly, the broadening of peaks observed with an increased Sm concentration may be attributed to a reduction in particle size⁶. A progressive decrease in the intensity of diffraction peaks is also noted with rising Sm concentration. This could be related to disorder within the

crystal lattice and a non-uniform distribution of Sm ions, potentially due to partial occupancy, resulting in weaker diffraction peaks. Moreover, specific diffraction peaks, such as those at 28.5° and 39.7° , undergo a reduction or disappearance, while a new peak emerges at 29.7° for $x_{Sm} = 1.0$.

Consistent behavior is observed at calcination temperatures of 200°C , 400°C , and 600°C , as illustrated in Figure.4.6. However, at 800°C , additional peaks emerge across all samarium concentrations, indicating a phase transformation. These diffraction peaks align well with trigonal tricalcium phosphate (TCP) using hexagonal axes with R3c:H symmetry group, as per ICDD No. 00-151-7238. According to the COD card, specific XRD peaks of TCP are identified at 27.7° , 29.5° , 30.9° , 34.2° , 46.8° , and 52.8° corresponding to the (3-14), (300), (20-10), (4-20), (4010), and (2020) lattice planes, respectively. Notably, a partial phase change to β -TCP occurs for pure HAp and every samarium concentration. The increase in Sm concentration enhances both the appearance and intensity of TCP diffraction peaks, with the exception of $x_{Sm} = 0.05$, which exhibits a high degree of phase transformation.

4.2 Optical Characterization

4.2.1 Photoluminescence Spectroscopy

The luminescent properties of Sm:HAp samples, at various samarium concentrations and calcination temperatures, were analyzed using photoluminescence (PL) spectroscopy. Figure 4.7 shows the PL spectra in the range of 400 to 800 nm at excitation of 405 nm, for Sm:HAp specimens at room temperature. Undoped hydroxyapatite exhibits no luminescence within this range, while Sm-doped samples display an emission spectrum with bands centered at 564 nm (moderate green), 600 nm (intense orange), 647 nm (intense red), and 709 nm (feeble red). These bands are assigned to electronic transitions within the Sm^{3+} ion: $^4\text{G}_{5/2} \rightarrow ^6\text{H}_{5/2}$, $^4\text{G}_{5/2} \rightarrow ^6\text{H}_{7/2}$, $^4\text{G}_{5/2} \rightarrow ^6\text{H}_{9/2}$, and $^4\text{G}_{5/2} \rightarrow ^6\text{H}_{11/2}$, respectively^{77,78}. Sm^{3+} reaches its strongest relative PL intensity at 600 nm in the visible domain, producing an orange light emission.

Among the various Sm concentrations, $x_{Sm} = 0.05$ has the highest emission intensity, indicating an optimal dopant concentration. However, as the concentration of Sm increases, a decline in luminescence is observed due to concentration quenching effects^{77,115}, a common phenomenon in rare earth ions within a host material¹¹⁶. The increase of Sm^{3+} ions corresponds to a reduction in inter-ionic distance and different lattice positions, intensifying interactions between light-emitting centers. Consequently, the dominance of energy transfer processes over radiative recombination leads to increased non-radiative decay or cross-relaxation^{77,116}. Additionally, the self-absorption mechanism, wherein emitted photons are re-absorbed within the material, contributes to the reduced luminescence. Notably, the relationship between dopant concentration and luminescence follows a non-linear trend; in this scenario, $x_{Sm} = 1.0$ exhibits the next highest PL intensity, followed closely by $x_{Sm} = 0.5$ and 0.1 , with minimal differences.

As illustrated in Figure 4.8, consistent trends are observed across Sm:HAp samples at calcination temperatures of 200°C , 400°C , 600°C , and 800°C . Minimal variability in intensity is evident across different dopant concentrations

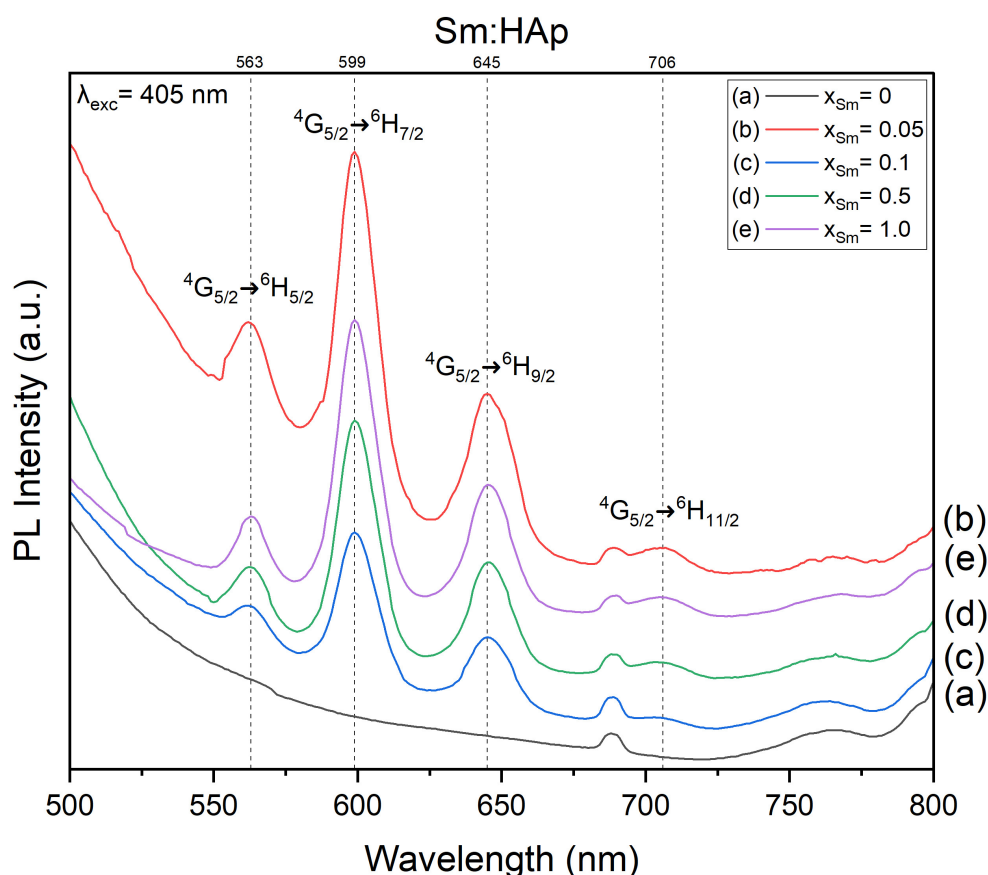


Figure 4.7: PL spectra of Sm:HAp at different samarium concentrations ($x_{Sm} = 0, 0.05, 0.1, 0.5, 1.0$).

at all temperatures. Furthermore, a minor increase in PL intensity is noted for specimens subjected to 600 °C calcination, accompanied by a reduction in the background contribution. Accordingly, the FTIR analysis reveals that calcination at 600 °C leads to the removal of carbonate and water, identified as impurities or defects in the crystal lattice. This removal induces a rearrangement of defects⁵⁰, facilitating a more favorable arrangement of Sm^{3+} ions into lattice sites and consequently enhancing luminescence. The most pronounced increase in PL intensity occurs at 800 °C. FTIR and XRD analyses indicate a phase transformation to β -TCP. Such phase transformation is typically related to structural and electronic alterations, along with changes in defect concentration, which may favor radiative recombination and enhance photoluminescence.

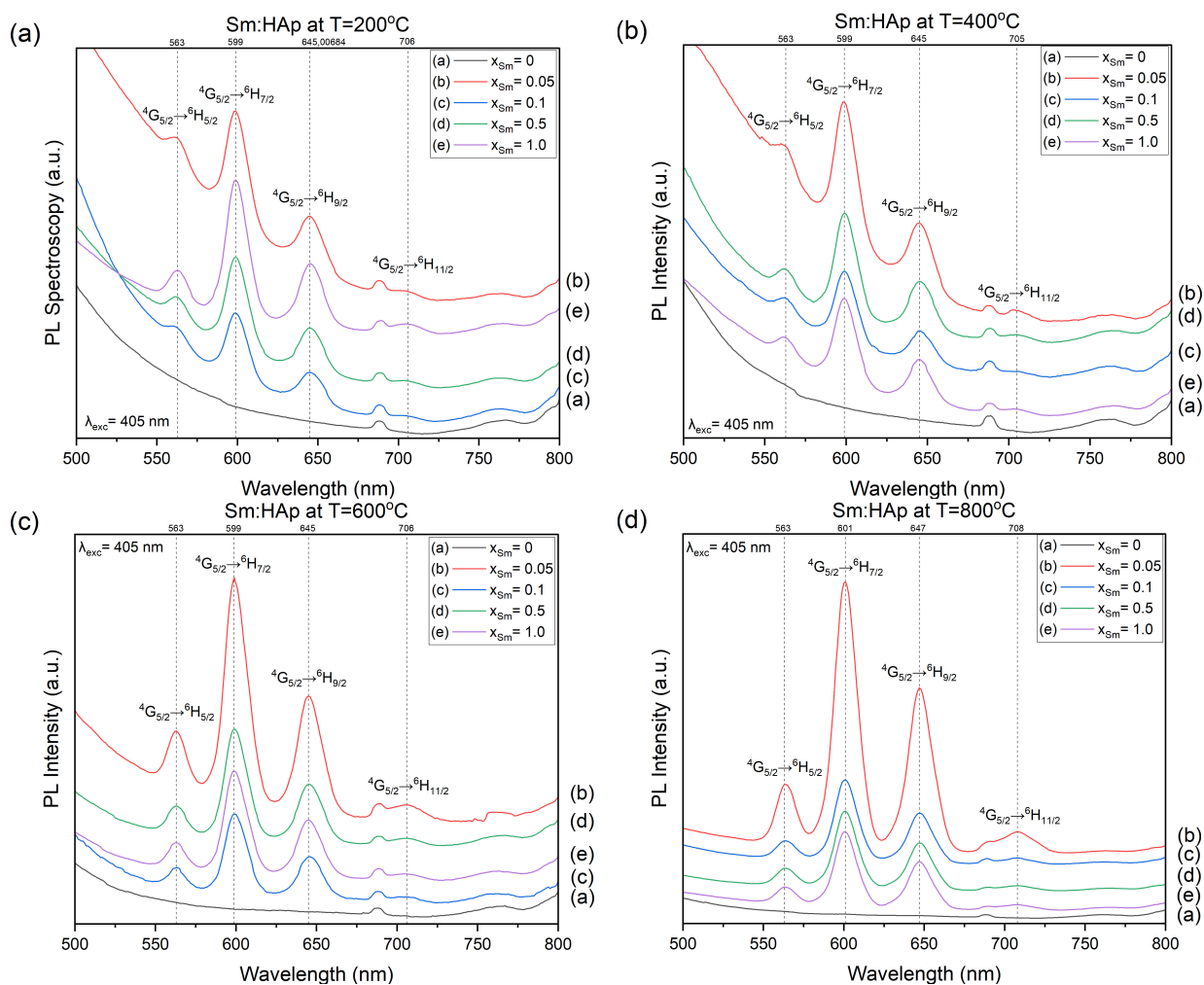


Figure 4.8: PL spectra of Sm:HAp at different samarium concentrations ($x_{Sm} = 0, 0.05, 0.1, 0.5, 1.0$) for different calcination temperatures: (a) 200 °C, (b) 400 °C, (c) 600 °C, and (d) 800 °C.

4.3 Morphological Characterization

4.3.1 Scanning Electron Microscopy

SEM was employed to investigate the morphology and physical characteristics of both uncalcined and calcined samples (Sm:HAp; $x_{Sm} = 0, 0.05, 0.5$) in the BSE mode at high magnifications of 83.3 kx. In uncalcined HAp (Figure 4.9 (a)), particles are notably dispersed, with some forming agglomerates ranging in size between 1.5 – 6 μm . These agglomerates exhibit an irregular shape, smooth edges, and a granular surface, composed of crystals

with a plate-like morphology. Interestingly, samarium-doped samples maintain the irregular morphology of HAp. Furthermore, there is no observable change in size for Sm-doped samples at $x_{Sm} = 0.05$ (Figure 4.9 (b)), while an increase to $16 \mu\text{m}$ is noted for $x_{Sm} = 0.5$ (Figure 4.9 (c)). However, there is a limited number of structures to determine a size average and tendency. Brighter particles are detected in $x_{Sm} = 0.5$ composites, possibly associated with the presence of Sm within the HAp matrix. Conversely, these brighter particles are less evident for $x_{Sm} = 0.05$, potentially attributed to its lower Sm concentration. Additionally, calcination to 800°C results in larger structures, with sizes ranging between $4 - 10 \mu\text{m}$. These agglomerates possess a more pronounced granular surface and consist of larger, rounded particles. The observed increase in size following calcination could be attributed to induced agglomeration caused by elevated temperatures or the partial phase transformation to TCP, as supported by FTIR and XRD analyses.

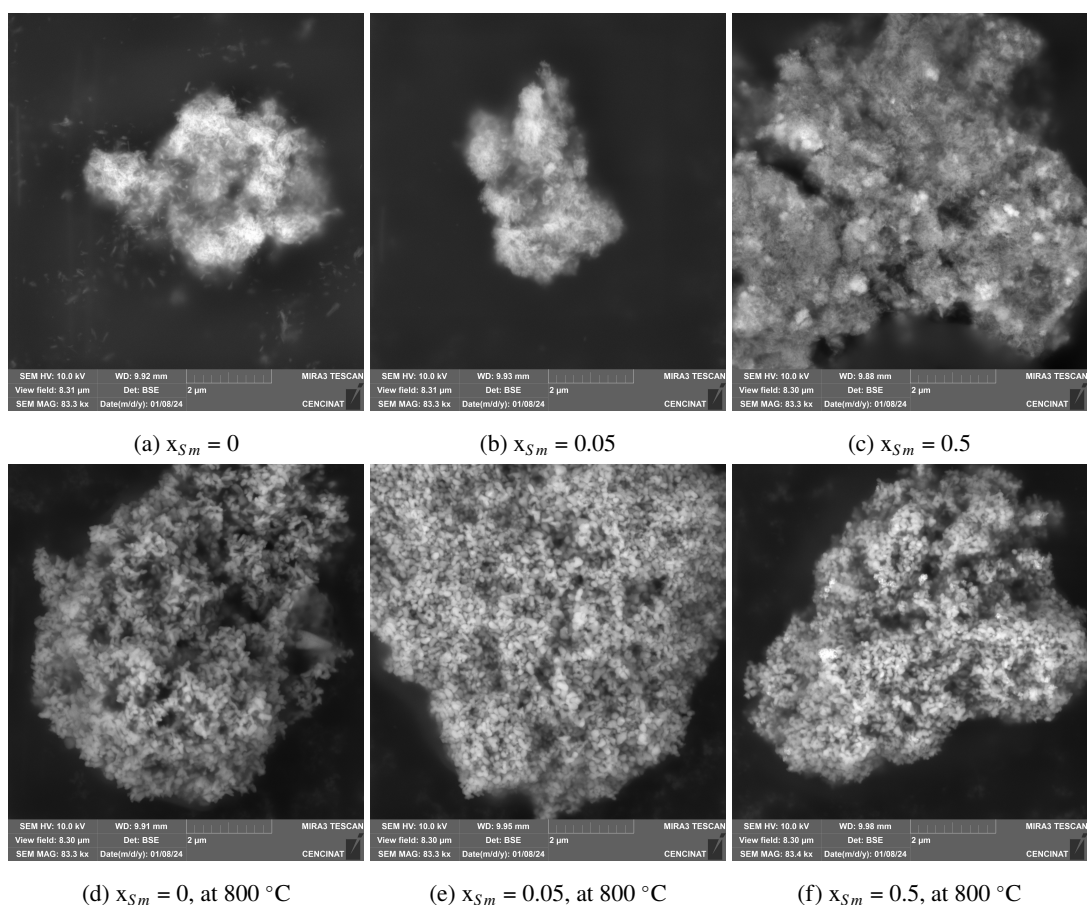


Figure 4.9: SEM images of (a), (b), (c) uncalcined and (d), (e), (f) calcined Sm:HAp samples at 800°C .

Energy Dispersive X-Ray Spectroscopy

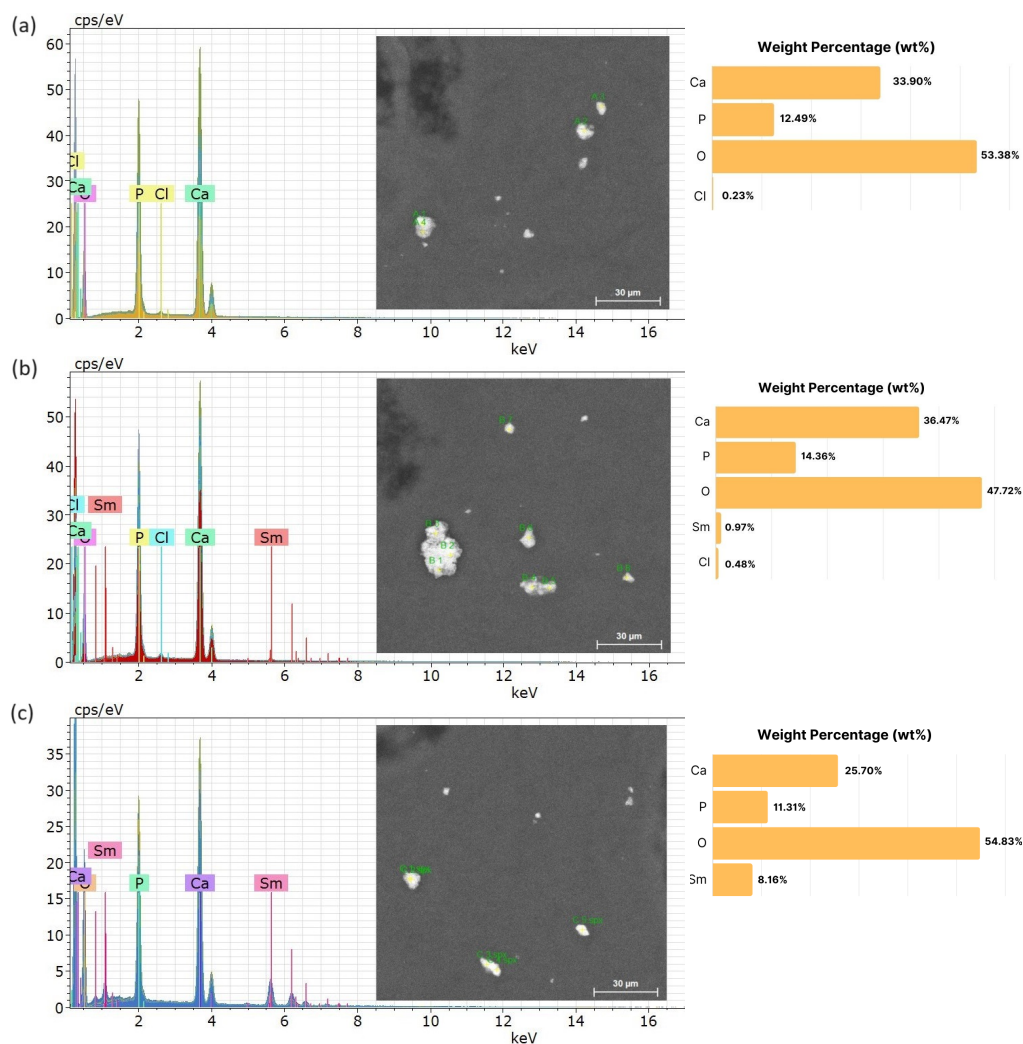


Figure 4.10: EDS microanalysis of Sm:HAp samples ($x_{Sm} = 0, 0.05$, and 0.5) at room temperature.

The EDS analysis highlighted the elemental and compositional characteristics of the Sm:HAp samples. Figure 4.10 illustrates the EDS spectrum for stoichiometric HAp and Sm:HAp at $x_{Sm} = 0.05$ and 0.5 . In Figure 4.10 (a), the presence of calcium (Ca), phosphorus (P), and oxygen (O) is confirmed, with a minimal proportion of chlorine (Cl). The flexibility of hydroxyapatite's structure, especially its affinity for substitutions, suggests the potential incorporation of chlorine as an impurity. Moreover, the EDS spectrum of samarium-doped specimens reveals the presence of Ca, P, O, and Sm. Notably, chlorine is absent in $x_{Sm} = 0.5$, indicating higher purity. Figure 4.10 (b) and Figure 4.10 (c) further confirm an increase in the weight percentage of Sm with higher Sm concentration in the

samples. Quantitative analysis is also provided for each sample. Elemental mapping (Figure 4.11) for $x_{Sm} = 0.5$, illustrates the even distribution of Ca, P, O, and Sm across the crystalline formations.

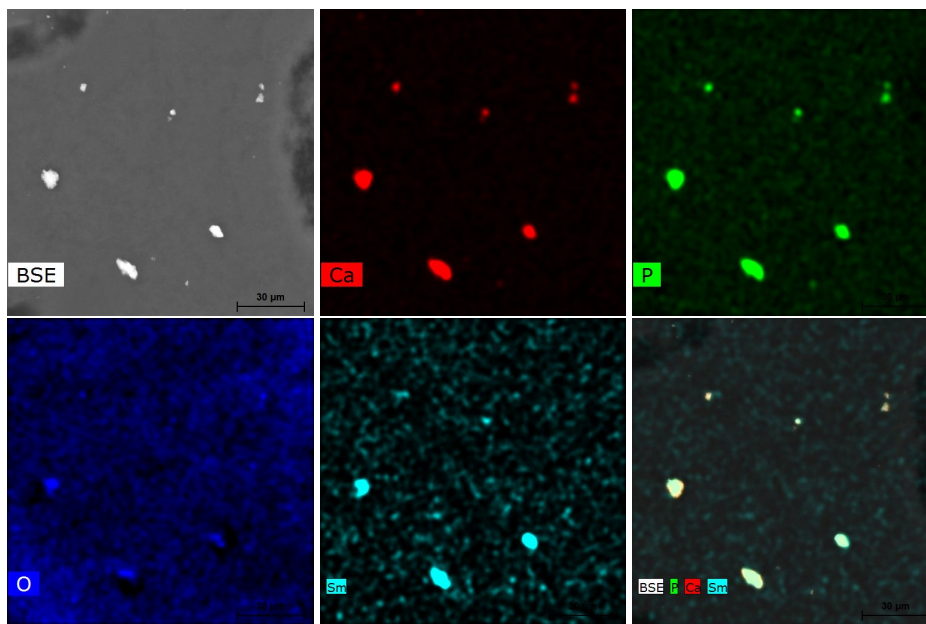


Figure 4.11: Elemental mapping of Sm:HAp ($x_{Sm} = 0.5$) samples at room temperature.

4.4 Cytotoxicity Studies

4.4.1 Trypan Blue

The Trypan Blue Dye Exclusion test was employed for a quantitative assessment of toxicity effects. This method determines cell viability based on the integrity of cell membranes. Neuroblastoma cell lines were exposed to Sm:HAp samples ($x_{Sm} = 0, 0.05, 0.1, 0.5, \text{ and } 1.0$), which were calcined at different temperatures for a 24-hour treatment.

As shown in Figure 4.12, the viability of cells exposed to both undoped and doped samples exhibited minimal changes. None of them showed complete cytotoxicity for SH-SY5Y. Pure hydroxyapatite, compared to the control with 93.26 % cell viability, showed a slight decrease at 92.63 %. For $x_{Sm} = 0.05, 0.1, 0.5, \text{ and } 1.0$ at room temperature, the viabilities were 88.78 %, 84.55 %, 84.99 %, and 83.98 %, respectively. This indicates a concentration-dependent reduction in cell viability for Sm:HAp samples. The same trend holds true across different temperatures. Although a slight decrease is evident for certain calcination temperatures, further analysis is needed to determine a definitive pattern.

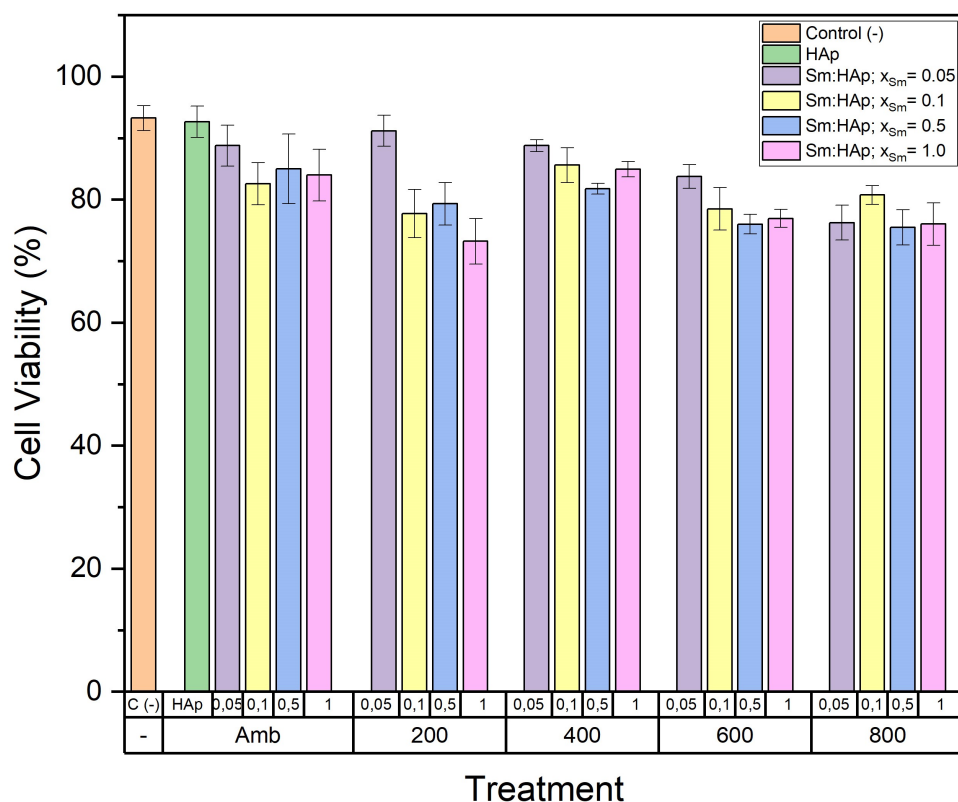


Figure 4.12: Biocompatibility assessment using Trypan Blue Dye Exclusion test: percentage of viable SH-SY5Y cells after a 24-hour incubation with Sm:HAp samples ($x_{Sm} = 0, 0.05, 0.1, 0.5, 1.0$) calcined at different temperatures. Results are expressed as the mean \pm SD.

The grain size and chemical composition of the administered treatment influence cell viability. Primarily, trypan blue is used to assess viability by measuring dye permeability on deceased cells, indicative of damaged cell membranes. By previous studies, Ln^{3+} ions can perforate the cell membrane even at low concentrations. Higher doses of Ln^{3+} ions activate apoptosis genes or cause DNA cleavage, resulting in observable cytotoxic effects at both cellular and animal in-vivo levels. At lower concentrations, lanthanides exhibit positive effects such as scavenging reactive oxygen species (ROS), providing cell protection, stabilizing the cytoskeleton, and enhancing immunological responses¹¹⁷. In this context, the dye exclusion test indicated a more significant reduction in the percentages of viable cells in cultures exposed to Sm:HAp compared to those exposed to pure HAp. EDS microanalysis further confirms high purity in both specimen types. Consequently, the incorporation of Sm induces neurotoxicity in a concentration-dependent manner, leading to an increased occurrence of cell death through apoptosis or the perforation of the cell membrane.

Biological effects are also influenced by various physical properties, including size, morphology, aggregation state, and surface texture. When considering grain size, the interaction between particles and the plasma membrane is crucial. Smaller particles exhibit efficient interfacial interaction with the cell membrane, leading to enhanced particle intake compared to larger particles. Consequently, smaller particles generally demonstrate lower toxicity, while larger particles tend to reduce cell viability. The impact of stimuli is influenced by factors such as mass concentration, effective interaction area, and total surface area. However, cytotoxicity may no longer be influenced by particle size when the dimensions surpass a threshold¹¹⁸. From the biocompatibility study, there is no defined cytotoxicity resulting from calcination temperature, i.e. particle size. SEM images revealed the tendency of particles in the sample to form agglomerates within the micrometer range. This observation raises the possibility that particle size may surpass a limit beyond which cytotoxicity is no longer primarily dependent on particle size. Hence, in the case of neurotoxicity on SH-SY5Y cells, the predominant factor seems to be the amount of Sm-content in the sample, rather than the particle size. Sm:HAp samples exhibit elevated cell viability and minimal neurotoxicity in terms of membrane integrity.

4.4.2 MTT Assay

MTT assay is a commonly applied technique in cell biology to assess cell viability and proliferation based on the metabolic activity of cells. Its applications include assessing the cytotoxicity of biomaterials, such as HAp and Sm:HAp, intended for biomedical use. SH-SY5Y cells were exposed for 24 hours to Sm:HAp samples ($x_{Sm} = 0, 0.05, 0.1, 0.5, \text{ and } 1.0$) calcined at different temperatures. The results are possible cell proliferation and reduced viability compared to the control group (100%).

As shown in Figure 4.13, the results of the MTT assay depict the influence of Sm concentration and calcination temperature on relative cell viability. Across all tested concentrations of the biomaterial, no complete neurotoxicity was observed. Undoped HAp approached the control value at 77.70 %, indicating a significant decrease in the percentage of viable cells. However, cell proliferation went to 97.7 %, 94.15 %, 127.20 %, and 42.70 % for $x_{Sm} = 0.05, 0.1, 0.5, \text{ and } 1.0$, respectively, at room temperature. These results may suggest low toxicity for $x_{Sm} = 0.05, 0.1$, proliferative capacity for $x_{Sm} = 0.5$, and high toxic effects for $x_{Sm} = 1.0$. Similar trends were observed for all calcination temperatures, indicating a concentration-dependent decline in cell viability in a non-linear trend. Low-concentration samples appear to exhibit proliferative capacity, while samples at $x_{Sm} = 1.0$ show a high death rate. Furthermore, there is no apparent tendency for neurotoxicity based on calcination temperature, i.e., particle size.

Cellular processes, including metabolic activity, may undergo alterations in the presence of a specific treatment. Generally, adverse biological effects are associated with the effective concentration of Ln^{3+} ions. Studies have shown that the radioactivity of these elements can stimulate growth at low doses. They demonstrate growth-promoting effects at very low concentrations but become inhibitory at higher concentrations¹¹⁷. This phenomenon was observed in Sm:HAp samples tested on the SH-SY5Y cell line, where low Sm-content ($\leq x_{Sm} = 0.5$) resulted in proliferative responses, while high Sm-content ($x_{Sm} = 1.0$) exhibited clear toxic effects.

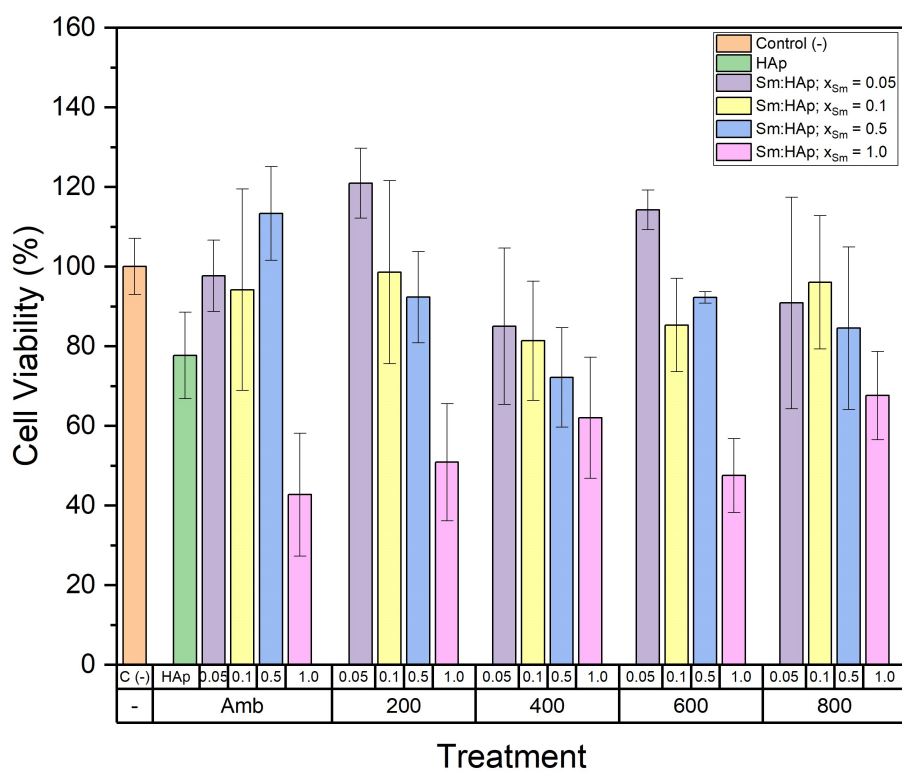


Figure 4.13: Biocompatibility assessment using MTT assay: percentage of viable SH-SY5Y cells after a 24-hour incubation with Sm:HAp samples ($x_{Sm} = 0, 0.05, 0.1, 0.5, 1.0$) calcined at different temperatures. Results are expressed as the mean \pm SEM.

Chapter 5

Conclusions & Outlook

Stoichiometric HAp and Sm:HAp were synthesized through the hydrothermal method with specific Sm concentration ($x_{Sm} = 0.05, 0.1, 0.5, 1.0$) and subjected to calcination at 200 °C, 400 °C, 600 °C, and 800 °C. Substitutional doping was intended by maintaining the (Ca + Sm)/P fixed to 1.67. The biomaterial underwent structural, morphological, compositional, and optical characterization to identify its properties.

Structural characterization confirmed the formation of HAp and the integration of Sm³⁺ ions within the structure without affecting the crystal lattice. FTIR and Raman spectroscopy presented the characteristic vibrational modes of pure apatite, including hydroxyl and phosphate groups. XRD analysis identified a hexagonal phase with P6₃/m spatial symmetry in HAp, a characteristic maintained across Sm:HAp samples. However, undoped and doped samples at 800 °C displayed a partial phase change to β -TCP. Morphologically, uncalcined specimens formed irregular agglomerates of plate-like crystals in the micrometer size, with calcination resulting in larger structures. EDS confirmed the presence and even distribution of samarium in Sm:HAp samples with relatively high purity. Optical properties were assessed through PL spectroscopy, revealing that $x_{Sm} = 0.05$ exhibited the highest emission intensity. However, higher Sm concentrations led to decreased luminescence due to concentration quenching effects. Additionally, specimens subjected to 600 °C and 800 °C calcination showed minor and major increases in PL intensity, respectively, attributed to impurity removal and phase transformation.

Cytotoxicity evaluation represents the initial stage in assessing biocompatibility of potential biomaterials. Trypan Blue Dye Exclusion and MTT assays serve as methods to assess cell viability, focusing on membrane integrity and metabolic activity, respectively. Following a 24-hour treatment exposure, Trypan Blue showed a minimal decrease in cell viability in SH-SY5Y cells. Moreover, there is a noticeable concentration-dependent reduction in the number of living cells. Simultaneously, the MTT assay revealed cell proliferation and low toxicity for samples with low Sm-content, while high Sm-content samples exhibited pronounced toxic effects. Overall, both results indicate that Sm:HAp induces cellular damage and death in SH-SY5Y cells in concentration-dependent manner.

The present study establishes a basis for more in-depth investigations into the neurotoxicity of samarium-doped hydroxyapatite systems. Future research could focus on synthesizing samples with lower dopant concentrations and exploring both short- and long-term cytotoxicity. Additional techniques, such as oxidative stress determination (ROS) and immunity assays, could be employed on specimens to examine their effects on oxidative stress and immune responses. Understanding the material's interaction with cells is crucial, including aspects like nanoparticle uptake and cytotoxic mechanisms. Employing imaging techniques such as electron and fluorescence microscopy may enable a detailed visualization of these interactions. Furthermore, exploring the material's potential in drug delivery systems for loading and releasing or evaluating its mechanical properties as coatings for load-bearing implants would contribute to broader applications.

Appendix A

Additional Information

X-ray Diffraction

Table A.1: Phase analysis for Sm:HAp samples calcined at 800 °C.

x_{Sm}	COD Card	Phase	Crystal Structure	Space Group	Cell Parameters
0	00-900-2214	Ca ₅ HO ₁₃ P ₃	Hexagonal	P6 ₃ /m	a = 9.4394 Å c = 6.8861 Å
	00-151-7235	Ca ₃ (PO ₄) ₂	Trigonal (hexagonal axes)	R3c:H	a = 10.4352 Å c = 37.4029 Å
0.05	00-431-7043	Ca ₁₀ H ₂ O ₂₆ P ₆	Hexagonal	P6 ₃ /m	a = 9.4190 Å c = 6.8812 Å
	00-151-7235	Ca ₃ (PO ₄) ₂	Trigonal (hexagonal axes)	R3c:H	a = 10.4352 Å c = 37.4029 Å
0.1	00-901-1094	Ca ₅ HO ₁₃ P ₃	Hexagonal	P6 ₃ /m	a = 9.4240 Å c = 6.8790 Å
	00-151-7235	Ca ₃ (PO ₄) ₂	Trigonal (hexagonal axes)	R3c:H	a = 10.4352 Å c = 37.4029 Å
0.5	00-901-1094	Ca ₅ HO ₁₃ P ₃	Hexagonal	P6 ₃ /m	a = 9.4240 Å c = 6.8790 Å
	00-151-7235	Ca ₃ (PO ₄) ₂	Trigonal (hexagonal axes)	R3c:H	a = 10.4352 Å c = 37.4029 Å
1.0	00-721-7892	Ca ₅ HO ₁₃ P ₃	Monoclinic	P1121/b	a = 9.4260 Å b = 18.8560 Å c = 6.8870 Å γ = 119.97°
	00-151-7235	Ca ₃ (PO ₄) ₂	Trigonal (hexagonal axes)	R3c:H	a = 10.4352 Å c = 37.4029 Å

PL Spectroscopy

Table A.2: PL peak intensities of Sm:HAp samples ($x_{Sm} = 0, 0.05, 0.1, 0.5, 1.0$) at different calcination temperatures

Wavelength (nm)	Electronic Transition	PL Intensity				
		$x_{Sm} = 0$	$x_{Sm} = 0.05$	$x_{Sm} = 0.1$	$x_{Sm} = 0.5$	$x_{Sm} = 1.0$
Room Temperature, 200°C, 400°C						
563	$^4G_{5/2} \rightarrow ^6H_{5/2}$	-	0.1901	0.1335	0.1159	0.1068
599	$^4G_{5/2} \rightarrow ^6H_{7/2}$	-	0.2758	0.1703	0.1895	0.2055
645	$^4G_{5/2} \rightarrow ^6H_{9/2}$	-	0.1541	0.1177	0.1183	0.0671
706	$^4G_{5/2} \rightarrow ^6H_{11/2}$	-	0.0765	0.0769	0.0679	0.0659
600°C						
563	$^4G_{5/2} \rightarrow ^6H_{5/2}$	-	0.1694	0.1036	0.1130	0.1065
599	$^4G_{5/2} \rightarrow ^6H_{7/2}$	-	0.3625	0.1712	0.2099	0.1971
645	$^4G_{5/2} \rightarrow ^6H_{9/2}$	-	0.2134	0.1175	0.1402	0.1352
706	$^4G_{5/2} \rightarrow ^6H_{11/2}$	-	0.0764	0.0670	0.0721	0.0670
800°C						
563	$^4G_{5/2} \rightarrow ^6H_{5/2}$	-	0.4278	0.1923	0.1820	0.1867
599	$^4G_{5/2} \rightarrow ^6H_{7/2}$	-	1.4693	0.5058	0.4764	0.4709
645	$^4G_{5/2} \rightarrow ^6H_{9/2}$	-	0.9244	0.3352	0.3127	0.3162
706	$^4G_{5/2} \rightarrow ^6H_{11/2}$	-	0.1854	0.1043	-	-

Cytotoxicity Studies

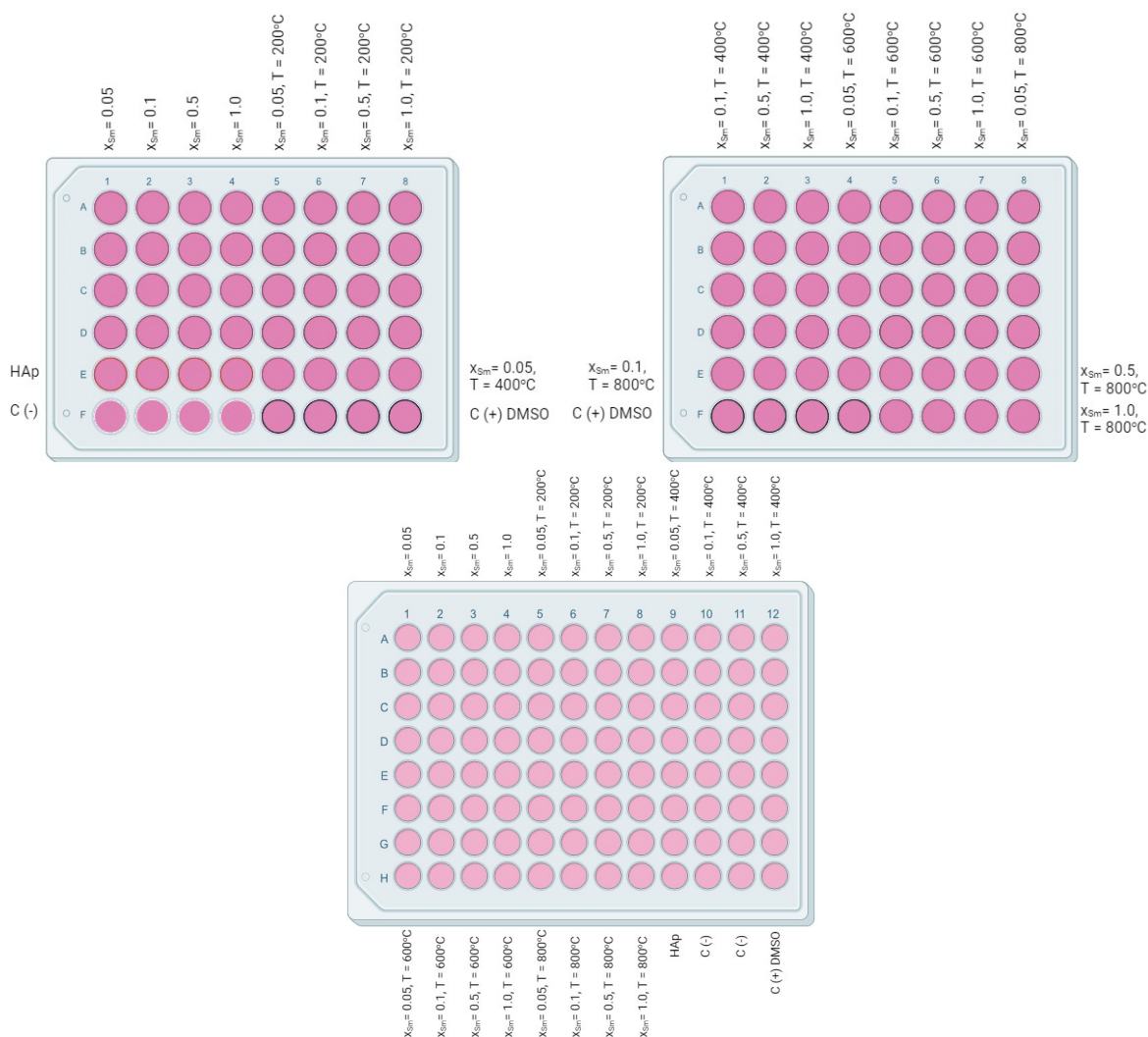


Figure A.1: 48-well plates for Trypan Blue and 96-well plate for MTT assays treatment positions.

Bibliography

- [1] Ciobanu, C. S.; Predoi, D.; Chapon, P.; Predoi, M. V.; Iconaru, S. L. Fabrication and Physico-Chemical Properties of Antifungal Samarium Doped Hydroxyapatite Thin Films. *Coatings* **2021**, *11*, 1466.
- [2] Iconaru, S.; Stanciu, G.; Hristu, R.; Ghita, R. Properties of samarium doped hydroxyapatite thin films deposited by evaporation. *Rom. Rep. Phys* **2017**, *69*, 508.
- [3] Iconaru, S. L.; Groza, A.; Gaiaschi, S.; Rokosz, K.; Raaen, S.; Ciobanu, S. C.; Chapon, P.; Predoi, D. Antimicrobial properties of samarium doped hydroxyapatite suspensions and coatings. *Coatings* **2020**, *10*, 1124.
- [4] Ciobanu, S. C.; Iconaru, S. L.; Predoi, D.; Prodan, A. M.; Predoi, M. V. Physico-chemical properties and in vitro antifungal evaluation of samarium doped hydroxyapatite coatings. *Coatings* **2020**, *10*, 827.
- [5] Jiang, Y.; Yuan, Z.; Huang, J. Substituted hydroxyapatite: a recent development. *Materials Technology* **2020**, *35*, 785–796.
- [6] Ciobanu, C.; Iconaru, S.; Popa, C.; Motelica-Heino, M.; Predoi, D. Evaluation of samarium doped hydroxyapatite, ceramics for medical application: Antimicrobial activity. *Journal of Nanomaterials* **2015**, *2015*, 14–14.
- [7] Nica, I. C.; Popa, M.; Marutescu, L.; Dinischiotu, A.; Iconaru, S. L.; Ciobanu, S. C.; Predoi, D. Biocompatibility and antibiofilm properties of samarium doped hydroxyapatite coatings: An in vitro study. *Coatings* **2021**, *11*, 1185.
- [8] Xicoy, H.; Wieringa, B.; Martens, G. J. The SH-SY5Y cell line in Parkinson's disease research: a systematic review. *Molecular neurodegeneration* **2017**, *12*, 1–11.
- [9] Kumar Teli, M.; Mutalik, S.; Rajanikant, G. Nanotechnology and nanomedicine: going small means aiming big. *Current pharmaceutical design* **2010**, *16*, 1882–1892.
- [10] Asha, A. B.; Narain, R. *Polymer science and nanotechnology*; Elsevier, 2020; pp 343–359.
- [11] Soares, S.; Sousa, J.; Pais, A.; Vitorino, C. Nanomedicine: principles, properties, and regulatory issues. *Frontiers in chemistry* **2018**, 360.

- [12] De Jong, W. H.; Borm, P. J. Drug delivery and nanoparticles: applications and hazards. *International journal of nanomedicine* **2008**, *3*, 133–149.
- [13] Zhang, X.-Q.; Xu, X.; Bertrand, N.; Pridgen, E.; Swami, A.; Farokhzad, O. C. Interactions of nanomaterials and biological systems: Implications to personalized nanomedicine. *Advanced drug delivery reviews* **2012**, *64*, 1363–1384.
- [14] Alharbi, K. K.; Al-Sheikh, Y. A. Role and implications of nanodiagnostics in the changing trends of clinical diagnosis. *Saudi journal of biological sciences* **2014**, *21*, 109–117.
- [15] Sim, S.; Wong, N. K. Nanotechnology and its use in imaging and drug delivery. *Biomedical reports* **2021**, *14*, 1–9.
- [16] Mukhtar, M.; Bilal, M.; Rahdar, A.; Barani, M.; Arshad, R.; Behl, T.; Brisc, C.; Banica, F.; Bungau, S. Nanomaterials for diagnosis and treatment of brain cancer: Recent updates. *Chemosensors* **2020**, *8*, 117.
- [17] Fiume, E.; Magnaterra, G.; Rahdar, A.; Verné, E.; Baino, F. Hydroxyapatite for biomedical applications: A short overview. *Ceramics* **2021**, *4*, 542–563.
- [18] Madupalli, H.; Pavan, B.; Tecklenburg, M. M. Carbonate substitution in the mineral component of bone: Discriminating the structural changes, simultaneously imposed by carbonate in A and B sites of apatite. *Journal of solid state chemistry* **2017**, *255*, 27–35.
- [19] Ressler, A.; Žužić, A.; Ivanišević, I.; Kamboj, N.; Ivanković, H. Ionic substituted hydroxyapatite for bone regeneration applications: A review. *Open Ceramics* **2021**, *6*, 100122.
- [20] Uskoković, V. The role of hydroxyl channel in defining selected physicochemical peculiarities exhibited by hydroxyapatite. *RSC advances* **2015**, *5*, 36614–36633.
- [21] Cacciotti, I. Cationic and anionic substitutions in hydroxyapatite. *Handbook of bioceramics and biocomposites* **2016**, 145–211.
- [22] Kay, M. I.; Young, R.; Posner, A. Crystal structure of hydroxyapatite. *Nature* **1964**, *204*, 1050–1052.
- [23] Arcos, D.; Vallet-Regí, M. Substituted hydroxyapatite coatings of bone implants. *Journal of Materials Chemistry B* **2020**, *8*, 1781–1800.
- [24] Zhu, Y.; Xu, L.; Liu, C.; Zhang, C.; Wu, N. Nucleation and growth of hydroxyapatite nanocrystals by hydrothermal method. *AIP Advances* **2018**, *8*.
- [25] Kalpana, M.; Nagalakshmi, R. Effect of reaction temperature and pH on structural and morphological properties of hydroxyapatite from precipitation method. *Journal of the Indian Chemical Society* **2023**, *100*, 100947.
- [26] Ibrahim, M.; Labaki, M.; Giraudon, J.-M.; Lamonier, J.-F. Hydroxyapatite, a multifunctional material for air, water and soil pollution control: A review. *Journal of hazardous materials* **2020**, *383*, 121139.

- [27] Shi, H.; Zhou, Z.; Li, W.; Fan, Y.; Li, Z.; Wei, J. Hydroxyapatite based materials for bone tissue engineering: A brief and comprehensive introduction. *Crystals* **2021**, *11*, 149.
- [28] Pu'ad, N. M.; Koshy, P.; Abdullah, H.; Idris, M.; Lee, T. Syntheses of hydroxyapatite from natural sources. *Heliyon* **2019**, *5*.
- [29] Pu'ad, N. M.; Haq, R. A.; Noh, H. M.; Abdullah, H.; Idris, M.; Lee, T. Synthesis method of hydroxyapatite: A review. *Materials Today: Proceedings* **2020**, *29*, 233–239.
- [30] Sadat-Shojai, M.; Khorasani, M.-T.; Dinpanah-Khoshdargi, E.; Jamshidi, A. Synthesis methods for nanosized hydroxyapatite with diverse structures. *Acta biomaterialia* **2013**, *9*, 7591–7621.
- [31] Pai, S.; Kini, S. M.; Selvaraj, R.; Pugazhendhi, A. A review on the synthesis of hydroxyapatite, its composites and adsorptive removal of pollutants from wastewater. *Journal of Water Process Engineering* **2020**, *38*, 101574.
- [32] Nayak, A. K. Hydroxyapatite synthesis methodologies: an overview. *International Journal of ChemTech Research* **2010**, *2*, 903–907.
- [33] Earl, J.; Wood, D.; Milne, S. Hydrothermal synthesis of hydroxyapatite. 2006.
- [34] Chiara, J. L. Z= 62, samario, Sm. El primer elemento químico con nombre de persona. **2019**,
- [35] Clementi, E.; Raimondi, D.; Reinhardt, W. P. Atomic screening constants from SCF functions. II. Atoms with 37 to 86 electrons. *The Journal of chemical physics* **1967**, *47*, 1300–1307.
- [36] Hammond, C. The elements. *Handbook of chemistry and physics* **2000**, *81*.
- [37] Shi, N.; Fort, D. Preparation of samarium in the double hexagonal close packed form. *Journal of the Less Common Metals* **1985**, *113*, 21–23.
- [38] Emsley, J. *Nature's building blocks: an AZ guide to the elements*; Oxford University Press, USA, 2011.
- [39] Chang, T.-L.; Zhao, M.-T.; Li, W.-J.; Wang, J.; Qian, Q.-Y. Absolute isotopic composition and atomic weight of samarium. *International Journal of Mass Spectrometry* **2002**, *218*, 167–172.
- [40] Murthy, K.; Virk, H. S. Luminescence phenomena: an introduction. *Defect and diffusion forum* **2014**, *347*, 1–34.
- [41] Báez-Rodríguez, A.; Zamora-Peredo, L.; García-González, L.; Hernández-Torres, J.; García-Hipólito, M.; Guzmán-Mendoza, J.; Falcony, C. LUMINESCENT MATERIALS: NATURAL AND SYNTHETIC MATERIALES LUMINISCENTES: NATURALES Y SINTÉTICOS. *Cienc. y Nanociencia* **2019**, *2*.
- [42] Gribkovskii, V. *Luminescence of Solids*; Springer, 1998; pp 1–43.

- [43] Eck, M. Performance enhancement of hybrid nanocrystal-polymer bulk heterojunction solar cells: aspects of device efficiency, reproducibility, and stability. Ph.D. thesis, Dissertation, Albert-Ludwigs-Universität Freiburg, 2014, 2014.
- [44] Kulmala, S.; Suomi, J. Current status of modern analytical luminescence methods. *Analytica Chimica Acta* **2003**, *500*, 21–69.
- [45] Book, G. Compendium of chemical terminology. *International Union of Pure and Applied Chemistry* **2014**, 528.
- [46] Holcombe, J. A. Fluorescence and Emission Spectroscopy, Theory. **1999**,
- [47] Huerta, V. J.; Fernández, P.; Gómez, V.; Graeve, O. A.; Herrera, M. Defect-related luminescence properties of hydroxyapatite nanobelts. *Applied Materials Today* **2020**, *21*, 100822.
- [48] Neacsu, I. A.; Stoica, A. E.; Vasile, B. S.; Andronescu, E. Luminescent hydroxyapatite doped with rare earth elements for biomedical applications. *Nanomaterials* **2019**, *9*, 239.
- [49] Machado, T. R.; Sczancoski, J. C.; Beltrán-Mir, H.; Nogueira, I. C.; Li, M. S.; Andrés, J.; Cordoncillo, E.; Longo, E. A novel approach to obtain highly intense self-activated photoluminescence emissions in hydroxyapatite nanoparticles. *Journal of Solid State Chemistry* **2017**, *249*, 64–69.
- [50] Gonzalez, G.; Costa-Vera, C.; Borrero, L. J.; Soto, D.; Lozada, L.; Chango, J. I.; Diaz, J. C.; Lascano, L. Effect of carbonates on hydroxyapatite self-activated photoluminescence response. *Journal of Luminescence* **2018**, *195*, 385–395.
- [51] Machado, T. R.; Sczancoski, J. C.; Beltrán-Mir, H.; Li, M. S.; Andres, J.; Cordoncillo, E.; Leite, E.; Longo, E. Structural properties and self-activated photoluminescence emissions in hydroxyapatite with distinct particle shapes. *Ceramics International* **2018**, *44*, 236–245.
- [52] Liu, S. Electronic structure of rare earth metals. *Handbook on the physics and chemistry of rare earths* **1978**, *1*, 233–335.
- [53] Riseberg, L.; Weber, M. Relaxation Phenomena in Rare-Earth Luminescence. *PROGRESS IN OPTICS* **1993**, *31*, 89–89.
- [54] Park, D. J.; Sekino, T.; Tsukuda, S.; Hayashi, A.; Kusunose, T.; Tanaka, S.-I. Photoluminescence of samarium-doped TiO₂ nanotubes. *Journal of Solid State Chemistry* **2011**, *184*, 2695–2700.
- [55] Sarıoğlu, A. O.; Yalçın, Ş. P.; Ceylan, Ü.; Aygün, M.; Kırpık, H.; Sönmez, M. Photoluminescence properties of samarium (III)-based complexes: Synthesis, characterization and single crystal X-ray. *Journal of Luminescence* **2020**, *227*, 117537.
- [56] Deng, R.; Yu, J.; Zhang, H.; Zhou, L.; Peng, Z.; Li, Z.; Guo, Z. Photoluminescence and electroluminescence properties of a samarium complex Sm (TTA) 3phen. *Chemical physics letters* **2007**, *443*, 258–263.

- [57] Chiang, C.-H.; Fang, Y.-C.; Lin, H.-Y.; Chu, S.-Y. Photoluminescence properties and thermal stability of samarium-doped barium phosphate phosphors. *Ceramics International* **2017**, *43*, 4353–4356.
- [58] Ashwini, K.; Pandurangappa, C.; Avinash, K.; Srinivasan, S.; Stefanakos, E. Synthesis, characterization and photoluminescence studies of samarium doped zinc sulfide nanophosphors. *Journal of Luminescence* **2020**, *221*, 117097.
- [59] Melo, L. L.; Castro Jr, G. P.; Gonçalves, S. M. Substantial intensification of the quantum yield of samarium (III) complexes by mixing ligands: Microwave-assisted synthesis and luminescence properties. *Inorganic chemistry* **2019**, *58*, 3265–3270.
- [60] Wang, S.; Xu, J.; Wang, J.; Wang, K.-Y.; Dang, S.; Song, S.; Liu, D.; Wang, C. Luminescence of samarium (III) bis-dithiocarbamate frameworks: codoped lanthanide emitters that cover visible and near-infrared domains. *Journal of Materials Chemistry C* **2017**, *5*, 6620–6628.
- [61] Adan, A.; Kiraz, Y.; Baran, Y. Cell proliferation and cytotoxicity assays. *Current pharmaceutical biotechnology* **2016**, *17*, 1213–1221.
- [62] Li, W.; Zhou, J.; Xu, Y. Study of the in vitro cytotoxicity testing of medical devices. *Biomedical reports* **2015**, *3*, 617–620.
- [63] Shafiee, M. A. M.; Asri, M. A. M.; Alwi, S. S. S. Review on the In Vitro Cytotoxicity Assessment in Accordance to the International Organization for Standardization (ISO). *Malaysian Journal of Medicine & Health Sciences* **2021**, *17*.
- [64] Masters, J. *Animal cell culture: a practical approach*; OUP Oxford, 2000; Vol. 232.
- [65] Freshney, R. I. *Culture of animal cells: a manual of basic technique and specialized applications*; John Wiley & Sons, 2015.
- [66] Farah, M. E.; Maia, M.; Penha, F. M.; Rodrigues, E. B. In *Retinal Pharmacotherapy*; Nguyen, Q. D., Rodrigues, E. B., Farah, M. E., Mieler, W. F., Eds.; W.B. Saunders: Edinburgh, 2010; pp 331–335.
- [67] Gupta, R.; Rajpoot, K.; Tekade, M.; Sharma, M. C.; Tekade, R. K. In *Pharmacokinetics and Toxicokinetic Considerations*; Tekade, R. K., Ed.; Advances in Pharmaceutical Product Development and Research; Academic Press, 2022; Vol. 2; pp 145–174.
- [68] Supino, R. MTT assays. *In vitro toxicity testing protocols* **1995**, 137–149.
- [69] Ghasemi, M.; Turnbull, T.; Sebastian, S.; Kempson, I. The MTT assay: utility, limitations, pitfalls, and interpretation in bulk and single-cell analysis. *International journal of molecular sciences* **2021**, *22*, 12827.
- [70] Sukhramani, P. S.; Sukhramani, P. S.; Tirthani, S. R.; Desai, S. A.; Suthar, M. P. Biological cytotoxicity evaluation of spiro [azetidine-2, 3'-indole]-2', 4 (1'H)-dione derivatives for anti-lung and anti-breast cancer activity. *Der Pharmacia Lettre* **2011**, *3*, 236–243.

- [71] Shastry, P.; Basu, A.; Rajadhyaksha, M. S. Neuroblastoma cell lines-A versatile in vitro model in neurobiology. *International journal of neuroscience* **2001**, *108*, 109–126.
- [72] Kovalevich, J.; Langford, D. Considerations for the use of SH-SY5Y neuroblastoma cells in neurobiology. *Neuronal cell culture: methods and protocols* **2013**, 9–21.
- [73] Xie, H.-r.; Hu, L.-s.; Li, G.-y. SH-SY5Y human neuroblastoma cell line: in vitro cell model of dopaminergic neurons in Parkinson's disease. *Chinese medical journal* **2010**, *123*, 1086–1092.
- [74] Shipley, M. M.; Mangold, C. A.; Szpara, M. L. Differentiation of the SH-SY5Y human neuroblastoma cell line. *JoVE (Journal of Visualized Experiments)* **2016**, e53193.
- [75] Zantye, P.; Fernandes, F.; Ramanan, S. R.; Kowshik, M. Rare earth doped hydroxyapatite nanoparticles for in vitro bioimaging applications. *Current Physical Chemistry* **2019**, *9*, 94–109.
- [76] Turculet, C. S.; Prodan, A. M.; Negoi, I.; Teleanu, G.; Popa, M.; Andronescu, E.; Beuran, M.; Stanciu, G. A.; Hristu, R.; Badea, M. L. Preliminary evaluation of the antifungal activity of samarium doped hydroxyapatite thin films. *Rom. Biotechnol. Lett.* **2018**, *23*, 13928–13932.
- [77] Chen, P.; Wang, F.; Qiao, Y.; Zhang, Z. Luminescence of samarium doped hydroxyapatite containing strontium: Effects of doping concentration. *Journal of Rare Earths* **2022**, *40*, 398–405.
- [78] Lv, Y.; Shi, Q.; Jin, Y.; Ren, H.; Qin, Y.; Wang, B.; Song, S. Preparation and Luminescent Properties of the antibacterial materials of the La³⁺ Doped Sm³⁺-Hydroxyapatite. 2018.
- [79] Movasaghi, Z.; Rehman, S.; ur Rehman, D. I. Fourier transform infrared (FTIR) spectroscopy of biological tissues. *Applied Spectroscopy Reviews* **2008**, *43*, 134–179.
- [80] Țucureanu, V.; Matei, A.; Avram, A. M. FTIR spectroscopy for carbon family study. *Critical reviews in analytical chemistry* **2016**, *46*, 502–520.
- [81] Talari, A. C. S.; Martinez, M. A. G.; Movasaghi, Z.; Rehman, S.; Rehman, I. U. Advances in Fourier transform infrared (FTIR) spectroscopy of biological tissues. *Applied Spectroscopy Reviews* **2017**, *52*, 456–506.
- [82] Berthomieu, C.; Hienerwadel, R. Fourier transform infrared (FTIR) spectroscopy. *Photosynthesis research* **2009**, *101*, 157–170.
- [83] Mohamed, M. A.; Jaafar, J.; Ismail, A.; Othman, M.; Rahman, M. *Membrane characterization*; Elsevier, 2017; pp 3–29.
- [84] Campanella, B.; Palleschi, V.; Legnaioli, S. Introduction to vibrational spectroscopies. *ChemTexts* **2021**, *7*, 1–21.
- [85] Graves, P.; Gardiner, D. Practical raman spectroscopy. *Springer* **1989**, *10*, 978–3.

- [86] Smith, E.; Dent, G. *Modern Raman spectroscopy: a practical approach*; John Wiley & Sons, 2019.
- [87] Kudelski, A. Analytical applications of Raman spectroscopy. *Talanta* **2008**, *76*, 1–8.
- [88] Moura, C. C.; Tare, R. S.; Oreffo, R. O.; Mahajan, S. Raman spectroscopy and coherent anti-Stokes Raman scattering imaging: prospective tools for monitoring skeletal cells and skeletal regeneration. *Journal of The Royal Society Interface* **2016**, *13*, 20160182.
- [89] Bunaciu, A. A.; UdrişTioiu, E. G.; Aboul-Enein, H. Y. X-ray diffraction: instrumentation and applications. *Critical reviews in analytical chemistry* **2015**, *45*, 289–299.
- [90] Whittig, L.; Allardice, W. X-ray diffraction techniques. *Methods of Soil Analysis: Part 1 Physical and Mineralogical Methods* **1986**, *5*, 331–362.
- [91] Hanawalt, J.; Rinn, H.; Frevel, L. Chemical analysis by X-ray diffraction: Classification and use of X-ray diffraction patterns. *Powder Diffraction* **1986**, *1*, 2–14.
- [92] Ramachandran, V. S.; Beaudoin, J. J. *Handbook of analytical techniques in concrete science and technology: principles, techniques and applications*; Elsevier, 2000.
- [93] Harrington, G. F.; Santiso, J. Back-to-Basics tutorial: X-ray diffraction of thin films. *Journal of Electroceramics* **2021**, *47*, 141–163.
- [94] Gilliland, G. Photoluminescence spectroscopy of crystalline semiconductors. *Materials Science and Engineering: R: Reports* **1997**, *18*, 99–399.
- [95] Mitrić, J. *Rare-Earth-activated Phosphors*; Elsevier, 2022; pp 69–84.
- [96] Torvik, J. T. *III-Nitride Semiconductors: Electrical, Structural and Defects Properties*; Elsevier, 2000; pp 17–49.
- [97] Singha, A.; Dhar, P.; Roy, A. A nondestructive tool for nanomaterials: Raman and photoluminescence spectroscopy. *American journal of physics* **2005**, *73*, 224–233.
- [98] Mohammed, A.; Abdullah, A. Scanning electron microscopy (SEM): A review. 2018.
- [99] Vernon-Parry, K. D. Scanning electron microscopy: an introduction. *III-Vs review* **2000**, *13*, 40–44.
- [100] Hafner, B. Scanning electron microscopy primer. *Characterization Facility, University of Minnesota-Twin Cities* **2007**, 1–29.
- [101] Seiler, H. Secondary electron emission in the scanning electron microscope. *Journal of Applied Physics* **1983**, *54*, R1–R18.
- [102] Goldstein, J. I.; Newbury, D. E.; Michael, J. R.; Ritchie, N. W.; Scott, J. H. J.; Joy, D. C. *Scanning electron microscopy and X-ray microanalysis*; Springer, 2017.

- [103] Ohring, M., Kasprzak, L., Eds. *Reliability and Failure of Electronic Materials and Devices (Second Edition)*, second edition ed.; Academic Press: Boston, 2015; pp 611–664.
- [104] Lloyd, G. E. Atomic number and crystallographic contrast images with the SEM: a review of backscattered electron techniques. *Mineralogical Magazine* **1987**, *51*, 3–19.
- [105] Hodoroaba, V.-D. *Characterization of Nanoparticles*; Elsevier, 2020; pp 397–417.
- [106] Abd Mutalib, M.; Rahman, M.; Othman, M.; Ismail, A.; Jaafar, J. *Membrane characterization*; Elsevier, 2017; pp 161–179.
- [107] Ciobanu, C. S.; Popa, C. L.; Predoi, D. Sm: HAp nanopowders present antibacterial activity against *Enterococcus faecalis*. *Journal of Nanomaterials* **2014**, *2014*, 6–6.
- [108] Frumosu, F.; Iconaru, S.; Predoi, D. Europium concentration effect of europium doped hydroxyapatite on proliferation of osteoblast cells. *Dig. J. Nanomater. Biostruct* **2011**, *6*, 1859–1865.
- [109] Afriani, F.; Dahlan, K.; Nikmatin, S.; Zuas, O. Alginate affecting the characteristics of porous beta-TCP/alginate composite scaffolds. *Journal of Optoelectronics and Biomedical Materials* **2015**, *7*, 67–76.
- [110] Başak, T.; Hasan, T.; Feray, B.; Enes, A. M.; Abdulgani, T.; Ivana, C.; Ahmet, H.; Kenan, Ç.; Di, S. A.; Adil, M. Synthesis and in vitro toxicity assessment of different nano-calcium phosphate nanoparticles. *Brazilian Archives of Biology and Technology* **2022**, *65*.
- [111] Garskaite, E.; Gross, K.-A.; Yang, S.-W.; Yang, T. C.-K.; Yang, J.-C.; Kareiva, A. Effect of processing conditions on the crystallinity and structure of carbonated calcium hydroxyapatite (CHAp). *CrystEngComm* **2014**, *16*, 3950–3959.
- [112] Ciobanu, C. S.; Iconaru, S. L.; Le Coustumer, P.; Constantin, L. V.; Predoi, D. Antibacterial activity of silver-doped hydroxyapatite nanoparticles against gram-positive and gram-negative bacteria. *Nanoscale Research Letters* **2012**, *7*, 1–9.
- [113] Cancelliere, R.; Rea, G.; Micheli, L.; Mantegazza, P.; Bauer, E. M.; El Khouri, A.; Tempesta, E.; Altomare, A.; Capelli, D.; Capitelli, F. Electrochemical and Structural Characterization of Lanthanum-Doped Hydroxyapatite: A Promising Material for Sensing Applications. *Materials* **2023**, *16*, 4522.
- [114] Timchenko, P.; Timchenko, E.; Pisareva, E.; Vlasov, M. Y.; Volova, L.; Frolov, O.; Kalimullina, A. Experimental studies of hydroxyapatite by Raman spectroscopy. *Journal of optical technology* **2018**, *85*, 130–135.
- [115] Tanko, Y.; Sahar, M.; Ghoshal, S. Prominent spectral features of Sm³⁺ ion in disordered zinc tellurite glass. *Results in Physics* **2016**, *6*, 7–11.
- [116] Mawlud, S. Q.; Ameen, M. M.; Sahar, M. R.; Mahraz, Z. A. S.; Ahmed, K. F. Spectroscopic properties of Sm³⁺ doped sodium-tellurite glasses: Judd-Ofelt analysis. *Optical materials* **2017**, *69*, 318–327.

-
- [117] Wang, K.; Li, R.; Cheng, Y.; Zhu, B. Lanthanides—the future drugs? *Coordination Chemistry Reviews* **1999**, *190*, 297–308.
- [118] Kolekar, T. V.; Thorat, N. D.; Yadav, H. M.; Magalad, V. T.; Shinde, M. A.; Bandgar, S. S.; Kim, J. H.; Agawane, G. L. Nanocrystalline hydroxyapatite doped with aluminium: A potential carrier for biomedical applications. *Ceramics International* **2016**, *42*, 5304–5311.